Analytical Models of Instantaneous Radiative Forcing across Opacity Regimes

PAULINA CZARNECKI,[a] LORENZO M. POLVANI,[a,b,c] AND ROBERT PINCUS[b]

[a] *Department of Applied Physics and Applied Mathematics, Columbia University, New York, New York*
[b] *Lamont-Doherty Earth Observatory, Palisades, New York*
[c] *Department of Earth and Environmental Sciences, Columbia University, New York, New York*

(Manuscript received 23 April 2025, in final form 10 September 2025, accepted 25 September 2025)

ABSTRACT: Radiative forcing by carbon dioxide depends on the difference between the surface and stratospheric temperature scaled by the logarithm of its concentration. This relationship arises due to the cooling-to-space theory or the $\tau = 1$ law, where all emission of infrared radiation originates from the atmospheric pressure level where the gas reaches sufficient optical thickness [in the case of carbon dioxide (CO_2), in the stratosphere]. Here, we develop theoretical understanding of forcing by other well-mixed greenhouse gases including methane (CH_4), nitrous oxide (N_2O), and chlorofluorocarbons (CFCs). Radiative forcing by an optically thin absorber (e.g., CFC-12) is governed by emission throughout the troposphere and scaled by the total change in gas concentration, such that a linear increase in gas abundance yields a linear increase in forcing. We examine the factors that control the magnitude of radiative forcing, demonstrating analytically that CFC-12 is a stronger per-molecule absorber than CO_2 due to its larger average cross section, rather than its bandwidth or spectral position. Application in idealized atmospheres with simplified lapse rates illustrates how radiative forcing by optically thin gases depends almost linearly on the lapse rate. Finally, gases that are both optically thin and optically thick across their absorption spectrum, such as N_2O and CH_4, can be understood as a combination of the two regimes, yielding a superlogarithmic relationship to concentration. Our theory is in excellent agreement with full-physics line-by-line calculations in atmospheres with and without spectral overlap by water vapor.

SIGNIFICANCE STATEMENT: The impact of a greenhouse gas on Earth's energy balance is critical to understanding Earth's climate. Optically thin gases, including ozone-depleting substances, exert an aggregate radiative forcing about a third of that of carbon dioxide despite their much lesser concentration. To understand the underlying physics, we derive an analytical model of radiative forcing by these gases, finding excellent agreement with reference calculations. We show that for a linear increase in gas concentration, there is a linear increase in radiative forcing by an optically thin gas, in contrast to the logarithmic response of carbon dioxide. Gases that are optically thick but less so than carbon dioxide, such as methane and nitrous oxide, act as a combination of thin and thick regimes.

KEYWORDS: Greenhouse gases; Longwave radiation; Radiative forcing

1. Introduction

Increasing the concentration of well-mixed greenhouse gases in the atmosphere increases longwave absorption and alters Earth's energy budget. The measure of the direct effect of gaseous absorption on the energy budget at the top of the atmosphere in a single atmospheric column is called instantaneous radiative forcing (IRF). Radiative forcing for a single profile can be calculated to arbitrary precision with line-by-line codes (Pincus et al. 2020) and predicted accurately with empirical models (Hansen et al. 1988; Forster et al. 2021; Huang et al. 2016). Theory, in contrast, lends interpretability to complicated spectral behavior and helps explain unexpected phenomena. Recently developed theories of radiative forcing by carbon dioxide (CO_2) are based on the insight that, in the most opaque regions of its main absorption band, CO_2 emits to space primarily in the stratosphere so that radiative forcing by CO_2 can be viewed as a swap of surface emission for stratospheric emission (Wilson and Gea-Banacloche 2012; Jeevanjee et al. 2021; Stevens and Kluft 2023). This insight, along with idealized representations of CO_2 spectroscopy, yields a simple analytical expression for $\mathcal{F}_{i\to f}^{CO_2}$, the IRF by CO_2 between initial and final mass concentrations q_i and q_f:

$$\mathcal{F}_{i\to f}^{CO_2} = 2l \ln\left(\frac{q_f}{q_i}\right)[B(\nu^*, T_s) - B(\nu^*, T_{\text{strat}})]. \quad (1)$$

Here, l describes the rate at which the logarithm of CO_2's absorption coefficient decreases with wavenumber, B is the hemispherically integrated Planck function evaluated at the band center $\nu^* = 667.5\,\text{cm}^{-1}$ (where peak absorption occurs), and T_s and T_{strat} are the surface and stratospheric temperature, respectively. This relationship explains why instantaneous radiative forcing is negative when the stratosphere is warmer than the surface, as occasionally happens on the Antarctic Plateau (Schmithüsen et al. 2015; Smith et al. 2018). It also provided the impetus needed to identify the majority of intermodel spread in CO_2 IRF in global climate models as being caused by biases in stratospheric temperature (He et al. 2023).

Carbon dioxide is the most opaque well-mixed greenhouse gas: The cumulative optical depth at the surface $\tau_s \gg 1$ across most of its band (Fig. 1a) so that the emission level $\tau = 1$ is within the atmosphere, allowing for simplified treatments of

Denotes content that is immediately available upon publication as open access.

Corresponding author: Paulina Czarnecki, pc2943@columbia.edu

DOI: 10.1175/JCLI-D-25-0233.1

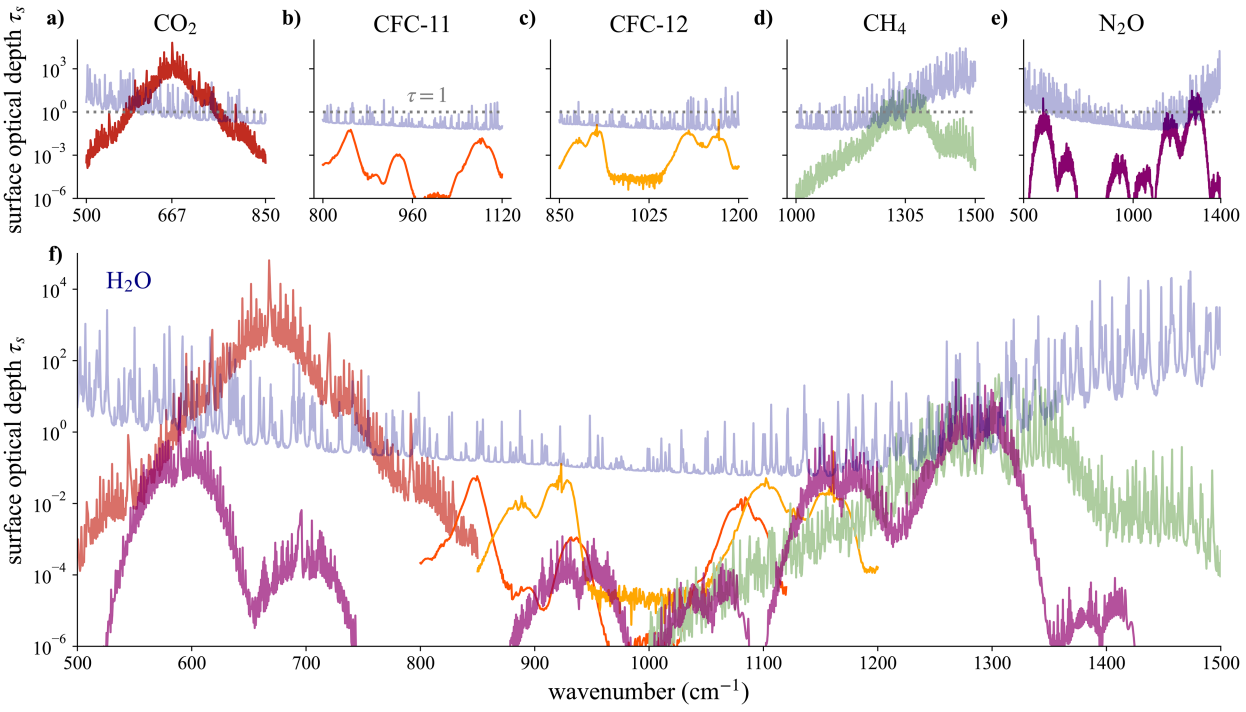

FIG. 1. The total atmospheric optical thickness at Earth's surface of a greenhouse gas at what are taken as present-day concentrations is shown: (a) CO_2 at 420 ppm (ppm), (b) CFC-11 at 240 ppt, (c) CFC-12 at 495 ppt, (d) CH_4 at 1650 ppb, and (e) N_2O at 332 ppb. (f) All six gases; line colors are made more transparent for readability. Spectral overlap by water vapor at 50% relative humidity is shown in blue, and the line above which a wavenumber is considered optically thick $\tau \approx 1$ is dotted in gray.

emission. CO_2's spectral structure is also remarkably regular and symmetric (Wordsworth et al. 2024), with the absorption coefficient falling off exponentially with wavenumber away from the maximum or band center; this behavior underlies the logarithmic dependence of radiative forcing on concentration.

Equation (1) cannot be applied to other well-mixed greenhouse gases (e.g., halocarbons, methane, or nitrous oxide) as its derivation relies on two properties that are specific to CO_2. One is that CO_2 is very optically thick and, in the simplest case, emits from the locally isothermal stratosphere in the most absorptive part of its band (Seeley 2018; Jeevanjee et al. 2021). The second is that CO_2 spectroscopy can be neatly idealized as symmetric exponential falloff from its maximum absorption in the band center—a log-linear triangle (Fig. 1a). These simplifications do not apply to other major well-mixed greenhouse gases. For instance, ozone-depleting substances chlorofluorocarbon (CFC)-11 and CFC-12 are optically thin throughout their band (Figs. 1b,c) yet exert an aggregate forcing almost a third of that of CO_2 ($\sim$0.4 W m^{-2} from 1950 to the present; Polvani et al. 2020; Hodnebrog et al. 2020). Methane and nitrous oxide exert a significant radiative forcing (Polvani et al. 2020; Forster et al. 2021), though they are not as optically thick as CO_2. Furthermore, methane and nitrous oxide exhibit complicated spectral absorption with multiple radiatively active bands with different optical thicknesses across the longwave spectrum (Figs. 1d,e).

Here, we develop a complete theory for local clear-sky longwave radiative forcing by greenhouse gases across opacity regimes, from very thin gases like the CFCs to the optically thick, well-understood CO_2. Our theory does not aim to compete with existing physical (e.g., Buehler et al. 2025; Pincus et al. 2016), statistical (e.g., Huang et al. 2016), or empirically derived (e.g., Byrne and Goldblatt 2014) models of radiative forcing but rather to extend the understanding of how characteristics of the forcing arise from spectral features. We begin by deriving an analytical model for radiative forcing by well-mixed, optically thin gases from solutions to the radiative transfer equation (section 2a). We show that instantaneous radiative forcing by optically thin gases is linear in concentration because band-average (linear) absorption, rather than (exponential) spectral features, governs its behavior. In section 2b, the theory identifies the factors that control the magnitude of the forcing by a given gas which allows us to demonstrate that CFC-12 is a much more powerful absorber, per-molecule, than CO_2 because its average cross-section size is larger than that of carbon dioxide (Ramanathan 1975; Shine 1991). The theory agrees well with full-physics line-by-line calculations of CFC-12 forcing in both idealized and realistic profiles with and without the presence of water vapor (sections 2c and 2d). Forcing by optically thin gases depends strongly on the entire atmospheric temperature profile, in contrast to CO_2, whose IRF depends only on the surface and stratospheric temperatures (section 2e). We further construct analytical models for radiative forcing by gases that are more opaque than the CFCs but more transparent than CO_2, providing a set of expressions that span opacity regimes (section 3a). We show that forcing by methane (section 3b)

and nitrous oxide (section 3c) can be understood as a linear combination of logarithmic and linear contributions.

2. Radiative forcing by optically thin gases

a. Theory

We seek an expression describing the instantaneous, clear-sky, top-of-the-atmosphere (TOA) radiative forcing by an arbitrary well-mixed optically thin gas, defined by optical depth $\tau < 1$ at each wavenumber throughout the atmosphere. We assume in this section that this gas is the only radiatively active species in the atmosphere; spectral overlap with water vapor is treated in section 2c. Monochromatic (per-wavenumber) instantaneous radiative forcing is defined as the difference between net downward TOA flux in an atmospheric column with initial concentration q_i and final concentration q_f. For longwave (thermal) forcing, net downward radiation is equal to negative outgoing longwave radiation (OLR):

$$\mathcal{F}_{i\to f}(\nu) = F_f^{\text{net}\downarrow}(\nu) - F_i^{\text{net}\downarrow}(\nu) = \text{OLR}_i(\nu) - \text{OLR}_f(\nu).$$

The OLR is given by Schwarzschild's two-stream equations (Schwarzschild 1906):

$$\mathcal{F}_{i\to f}(\nu) = \left\{B(T_s)e^{-\tau_{i,s}} - \int_{p_{\text{TOA}}}^{p_s} B(p)\frac{d}{dp}[e^{-\tau_i(p)}]dp\right\} - \left\{B(T_s)e^{-\tau_{f,s}} - \int_{p_{\text{TOA}}}^{p_s} B(p)\frac{d}{dp}[e^{-\tau_f(p)}]dp\right\},$$

where B is the hemispherically integrated Planck function at temperature T or pressure p and τ is the cumulative optical thickness profile including a diffusivity constant. Subscripts s and TOA denote the surface and the top of the atmosphere, respectively. Though the Planck function and optical thickness are monochromatic, we omit ν from our notation for convenience.

Combining like terms and defining the change in transmissivity between gas concentrations q_i and q_f as $\Delta_{i\to f}\mathcal{T}(p) := \mathcal{T}_i(p) - \mathcal{T}_f(p) = e^{-\tau_i(p)} - e^{-\tau_f(p)}$,

$$\mathcal{F}_{i\to f}(\nu) = B(T_s)\Delta_{i\to f}\mathcal{T}_s - \int_{p_{\text{TOA}}}^{p_s} B(p)\frac{d}{dp}[\Delta_{i\to f}\mathcal{T}(p)]dp. \quad (2)$$

To compute the vertical integral in Eq. (2), we assume the Planck function can be approximated with a bulk atmospheric emission constant $\overline{B} \approx B(p)$, which yields

$$\mathcal{F}_{i\to f}(\nu) \approx B(T_s)\Delta_{i\to f}\mathcal{T}_s - \overline{B}\int_{p_{\text{TOA}}}^{p_s}\frac{d}{dp}[\Delta_{i\to f}\mathcal{T}(p)]dp = B(T_s)\Delta_{i\to f}\mathcal{T}_s - \overline{B}\Delta_{i\to f}\mathcal{T}_s. \quad (3)$$

We take $\overline{B}$ to be the weighted-average Planck function in pressure, i.e.,

$$\overline{B} = \frac{\int_{p_{\text{TOA}}}^{p_s}\omega(p)B(p)dp}{\int_{p_{\text{TOA}}}^{p_s}\omega(p)dp}. \quad (4)$$

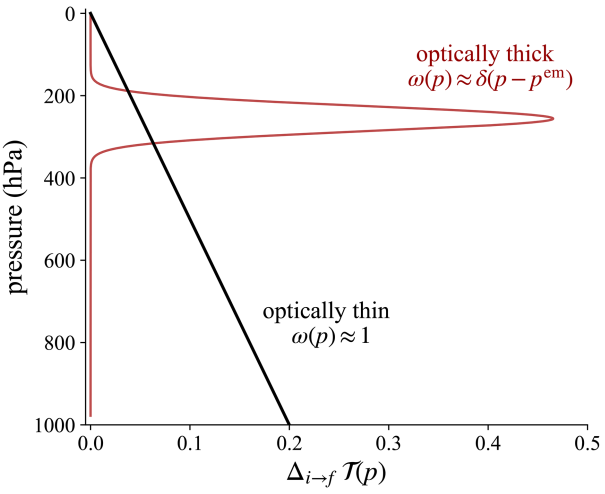

FIG. 2. The schematic illustrates the change in transmissivity $\Delta_{i\to f}\mathcal{T}$, which informs the weighting function in Eq. (4). For an optically thick gas, the peak in transmission occurs at the emission pressure p^{em} and can be approximated by a Dirac delta function at that pressure level (purple). Conversely, an optically thin gas leaves all atmospheric levels transparent to thermal radiation, and the weighting function can be constant (black).

In atmospheres with arbitrary thermal structure, $\overline{B}$ must be calculated numerically (we show results for idealized profiles in section 2e). The weighting function $\omega(p)$ is carefully chosen to capture the levels where atmospheric emission originates. The difference in transmissivity between two gas concentrations $\Delta_{i\to f}\mathcal{T}(p)$ informs the choice of weighting function.

For optically thick gases, $\Delta_{i\to f}\mathcal{T}(p)$ maximizes at one emission pressure p^{em} where $\tau = \tau^{\text{em}}$. The emission optical thickness τ^{em} defines the threshold at which a gas can be considered optically thick and is approximately $\tau^{\text{em}} \approx 1$, though we follow Jeevanjee et al. (2021) to calculate this value in detail, discussed in the appendix, section a. This emission pressure framework is shown schematically in purple in Fig. 2, where a very optically thick gas emits entirely at a low pressure level. In this case, $\mathcal{F}$ is well approximated by choosing ω to be a Dirac delta function centered at p^{em}. This choice and the assumption that the emission temperature $T^{\text{em},i} = T^{\text{em},f}$, followed by a geometric spectral integration, yield Eq. (1) (see section 3a; Dufresne et al. 2020; Wilson and Gea-Banacloche 2012; Jeevanjee and Fueglistaler 2020a).

For optically thin gases, however, the weighting function can be directly derived: $\Delta\mathcal{T}$ is linear in pressure (Dufresne et al. 2020), so that $(d\Delta\mathcal{T})/dp$ is approximately constant, and the weighting function $\omega \approx 1$ (Fig. 2, black). Mathematically, we can show that $\omega \approx 1$ from the second term in Eq. (2). If $(d/dp)[\Delta_{i\to f}\mathcal{T}(p)]$ is approximately constant,

$$\int_{p_{\text{TOA}}}^{p_s} B(p)\frac{d}{dp}[\Delta_{i\to f}\mathcal{T}(p)]dp \approx \frac{d}{dp}[\Delta_{i\to f}\mathcal{T}(p)]\int_{p_{\text{TOA}}}^{p_s} B(p)dp. \quad (5)$$

Replacing $(d\Delta_{i\to f}\mathcal{T})/dp$ with its finite difference,

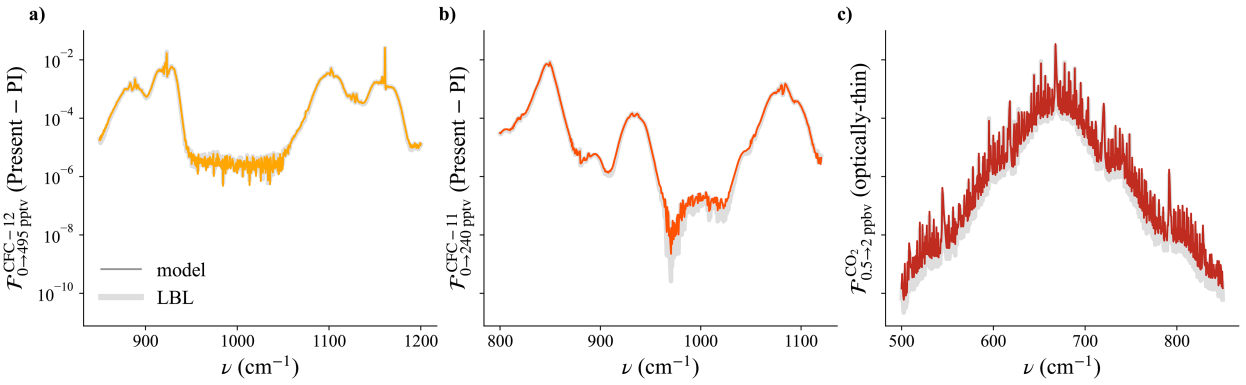

FIG. 3. The LBL (solid gray) and modeled (colored lines) forcings exerted by (a) preindustrial–present-day CFC-12 concentrations (yellow), (b) preindustrial–present-day CFC-11 concentrations (orange), and (c) a quadrupling of optically thin CO_2 (red), calculated via Eq. (9) in a single standard tropical atmosphere.

$$\frac{d}{dp}[\Delta_{i\to f}\mathcal{T}(p)]\int_{p_{\mathrm{TOA}}}^{p_s} B(p)dp \approx \frac{\Delta_{i\to f}\mathcal{T}_s - \Delta_{i\to f}\mathcal{T}_{\mathrm{TOA}}}{p_s - p_{\mathrm{TOA}}}\int_{p_{\mathrm{TOA}}}^{p_s} B(p)dp \tag{6}$$

$$= \Delta_{i\to f}\mathcal{T}_s \frac{\int_{p_{\mathrm{TOA}}}^{p_s} B(p)dp}{\int_{p_{\mathrm{TOA}}}^{p_s} dp} \tag{7}$$

$$= \Delta_{i\to f}\mathcal{T}_s \overline{B}, \tag{8}$$

identical to the second term in Eq. (3) with $\omega = 1$. This weighting function is similar to those used in other contexts (Stephens 1994; Liou 2002; Huang and Bani Shahabadi 2014; Dufresne et al. 2020), though as ω is derived from the expression of IRF, it characterizes a change in gas emission rather than at a given gas concentration. Additionally, pressure averaging the tropospheric Planck function ties the magnitude of Planck emission to the atmospheric mass distribution and is mathematically derived above. For this reason, in practice, we numerically integrate Eq. (4) to the tropopause rather than the TOA; nonetheless, optical depth is calculated throughout the depth of the atmosphere, and we only consider TOA radiative forcing in this work.

The fact that $\tau \ll 1$ also allows us to approximate the transmissivity $\mathcal{T} = e^{-\tau}$ as $\mathcal{T} \approx 1 - \tau$ (e.g., Dufresne et al. 2020). Then, $\Delta_{i\to f}\mathcal{T} \approx \Delta_{f\to i}\tau$ and the monochromatic IRF takes the simple form:

$$\mathcal{F}_{i\to f}(\nu) = [B(T_s) - \overline{B}]\Delta_{f\to i}\tau_s. \tag{9}$$

Equation (9) demonstrates that radiative forcing by an optically thin gas results from the replacement of emission from the surface $[B(T_s)]$ by the mass-weighted emission of the atmosphere $(\overline{B})$ scaled by the total change in atmospheric optical depth $(\Delta\tau_s)$.

Figure 3 shows spectrally resolved IRF for preindustrial–present-day concentrations of CFC-12 (Fig. 3a) and CFC-11 (Fig. 3b) and a quadrupling of CO_2 from 0.5 to 2 parts per billion by volume (ppbv) so that it is optically thin throughout the band (Fig. 3c). While this concentration of CO_2 is not realistic on Earth, the calculation demonstrates that Eq. (9) applies to any optically thin gas. Also shown are full-physics line-by-line Atmospheric Radiative Transfer Simulator (ARTS) computations (Buehler et al. 2022, 2025), which we take as an exact reference at high spectral resolution. ARTS uses the high-resolution transmission (HITRAN) spectroscopic dataset (Gordon et al. 2017; Kochanov et al. 2019) to calculate the monochromatic optical depth τ_s. Here and throughout the paper, Schwarzschild's equations are solved directly using Eq. (2). Calculations are clear-sky, longwave only, disregard scattering, and assume perfect blackbody emission from the surface. Single-column calculations assume a standard tropical temperature profile with a surface temperature of 286 K and a temperature profile following a moist adiabatic lapse rate. Our theoretical model (color) tracks line-by-line (LBL) forcing (gray) well for individual wavenumbers.

Radiative forcing is the spectral integral of Eq. (9). To integrate, we first assume that the absorption coefficient κ is independent of temperature and pressure. We ignore the second-order effects of temperature and pressure broadening in favor of analytical tractability, as we find good agreement with line-by-line calculations even in their absence. Then, cumulative optical depth τ at given gas concentration q is

$$\tau(p, \nu, q) = \int_{p_{\mathrm{TOA}}}^{p} D\kappa_{\mathrm{ref}}(\nu)\frac{q}{g}dp = D\kappa_{\mathrm{ref}}(\nu)\frac{q}{g}p, \tag{10}$$

where κ_{ref} ($\mathrm{m^2\ kg^{-1}}$) is the mass absorption coefficient at a reference pressure (Jeevanjee et al. 2021), q is the mass concentration of the gas ($\mathrm{kg\ kg^{-1}}$), g is the acceleration due to gravity ($\mathrm{m\ s^{-2}}$), and integration is performed from the top of the atmosphere to the given pressure level p (Pierrehumbert 2010). Though a diffusivity constant of $D = 1.66$ has long been known to minimize errors in computing longwave fluxes in nonscattering media under most conditions (Elsasser 1942; Goody and Young 1964), here we use $D = 2$ to match the default two-stream coefficient used by our reference line-by-line code ARTS.

Substituting Eq. (10) for τ_s in Eq. (9) allows us to write the spectral integral of forcing as

$$\mathcal{F}_{i\to f} = (q_f - q_i)\frac{Dp_s}{g}\int_\nu [B(T_s, \nu) - \overline{B}(\nu)]\kappa_{\text{ref}}(\nu)d\nu.$$

Next, the Planck function is evaluated at the wavenumber ν^* at the band center (e.g., CFC-12 is radiatively active between 800 and 1200 cm^{-1}; Fig. 1b), as the Planck function is generally monotonic in a given band, and so the band center value is equal to its mean (Jeevanjee et al. 2021):

$$\mathcal{F}_{i\to f} = [B(T_s, \nu^*) - \overline{B}(\nu^*)](q_f - q_i)\frac{Dp_s}{g}\int_\nu \kappa_{\text{ref}}(\nu)d\nu.$$

Now, only κ_{ref} varies spectrally. Its integral κ^*_{ref} is its spectral average: $\kappa^*_{\text{ref}} = [\int_\nu \kappa_{\text{ref}}(\nu)d\nu]/\delta\nu$, where $\delta\nu$ is the spectral width of the band. In other words, the rectangle with the height κ^*_{ref} and width $\delta\nu$ has the same area as the spectrally resolved κ_{ref}. Making this substitution,

$$\mathcal{F}_{i\to f} = [B(T_s, \nu^*) - \overline{B}(\nu^*)](q_f - q_i)\frac{Dp_s}{g}\kappa^*_{\text{ref}}\,\delta\nu.$$

If we define $\tau^*(p) := \kappa^*_{\text{ref}}(Dp/g)$ as the band-average optical thickness profile at unit mass concentration ($q = 1$ kg kg^{-1}), we can write the spectrally integrated optically thin gas forcing as a function of $\Delta q = (q_f - q_i)$:

$$\mathcal{F}_{i\to f} = [B(T_s, \nu^*) - \overline{B}(\nu^*)]\Delta q\,\tau^*_s\,\delta\nu. \tag{11}$$

Forcing by optically thin gases differs from forcing by carbon dioxide at present-day (optically thick) concentrations in two key ways. First, $\mathcal{F}_{i\to f} \propto (q_f - q_i)$, i.e., radiative forcing by an optically thin gas is linear in gas concentration independent of the shape of the absorption coefficient; in fact, Eq. (9) demonstrates that $\mathcal{F}$ is monochromatically linear in τ. Second, radiative forcing by optically thin gases depends on the difference between the surface temperature and the entire mass-weighted temperature profile rather than the temperature difference between the surface and stratosphere. Physically, the linearity of optically thin gas forcing follows from the fact that all wavenumbers substantially contributing to the total radiative forcing have an optical depth of about the same order of magnitude, $\tau \sim \mathcal{O}(0.1)$, and the contribution of wavenumbers where $\tau \ll 1$ is negligible. Thus, the integral (or sum) of these contributions is linear with Δq. Conversely, in the optically thick regime, all wavenumbers with $\tau > 1$ contribute to the forcing with varying orders of magnitude, the distribution of which is determined by the shape of the absorption coefficient. Consequently, IRF by CO_2 at Earth-like concentrations is logarithmic in concentration because of the exponentially decreasing shape of its absorption coefficient.

Line-by-line calculations in Fig. 4 confirm the linear relationship between Δq and $\mathcal{F}$ for CFC-12 (yellow), CFC-11 (orange), and optically thin CO_2 (red). The gray line between smallest and largest forcing by each gas illustrates the near-perfect linearity of the LBL forcing in concentration. While Eq. (11) or a regression would provide a similar result, we use the simplest fit to demonstrate the linear functional form independently of our model. Though CO_2 is presently many orders of magnitude more abundant than CFCs, in Fig. 4, the IRF is plotted at equivalent concentrations of each gas to illustrate that linear behavior for small τ applies across gas species. The slope of the linear response is determined by the band-average absorption coefficient, an idea we discuss next in section 2b.

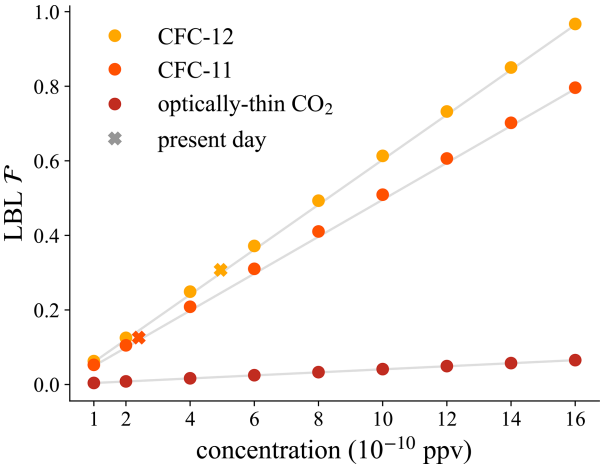

FIG. 4. LBL forcing by CFC-12 (yellow), CFC-11 (orange), and CO_2 (red) in a single tropical column for small concentrations away from zero (hundreds of pptv). Cross-shaped markers denote the forcing at present-day concentrations of CFC-11 and CFC-12. The gray line gives the linear fit between the smallest and largest forcings for each gas, demonstrating the linearity of the forcing in concentration.

b. *Band-average CFC-12 cross section controls its radiative efficiency*

Though CFC-12 is many orders of magnitude less concentrated in the present day than CO_2, CFC-12 exerts a forcing only a factor of three smaller over the period 1950–2005 (Polvani et al. 2020; Hodnebrog et al. 2020); Fig. 4 shows that for the same concentrations, IRF by CFC-12 and CFC-11 is much larger than that by CO_2. What determines the difference in forcing magnitude between CFC-12 and CO_2? Radiative forcing in a single column is governed by four factors: the concentration change Δq, the size of the absorption cross-section κ^*_{ref}, the magnitude of the Planck function where the gas emits $B(\nu^*)$, and the width of the band where the gas emits $\delta\nu$ (see also Shine 1991; Pinnock et al. 1995). In Fig. 5, we change each factor individually to determine which has the largest impact.

To compare CFC-12 and CO_2 using the optically thin theory, we study CO_2 at preindustrial–present-day CFC-12 concentrations [0–495 parts per trillion by volume (pptv)], where it is optically thin across its band. For a given atmospheric profile, the resulting CO_2 radiative forcing is much smaller than CFC-12 forcing at the same concentrations (Figs. 5a,d). When CFC-12 is moved to emit from the CO_2 band center, from $\nu^* = 1025$to $\nu^* = 667\,\text{cm}^{-1}$, the forcing increases modestly (Fig. 5b) as the Planck function peaks around 560 cm^{-1}. However, replacing the band-mean CFC-12 absorption coefficient κ^*_{ref} with the CO_2

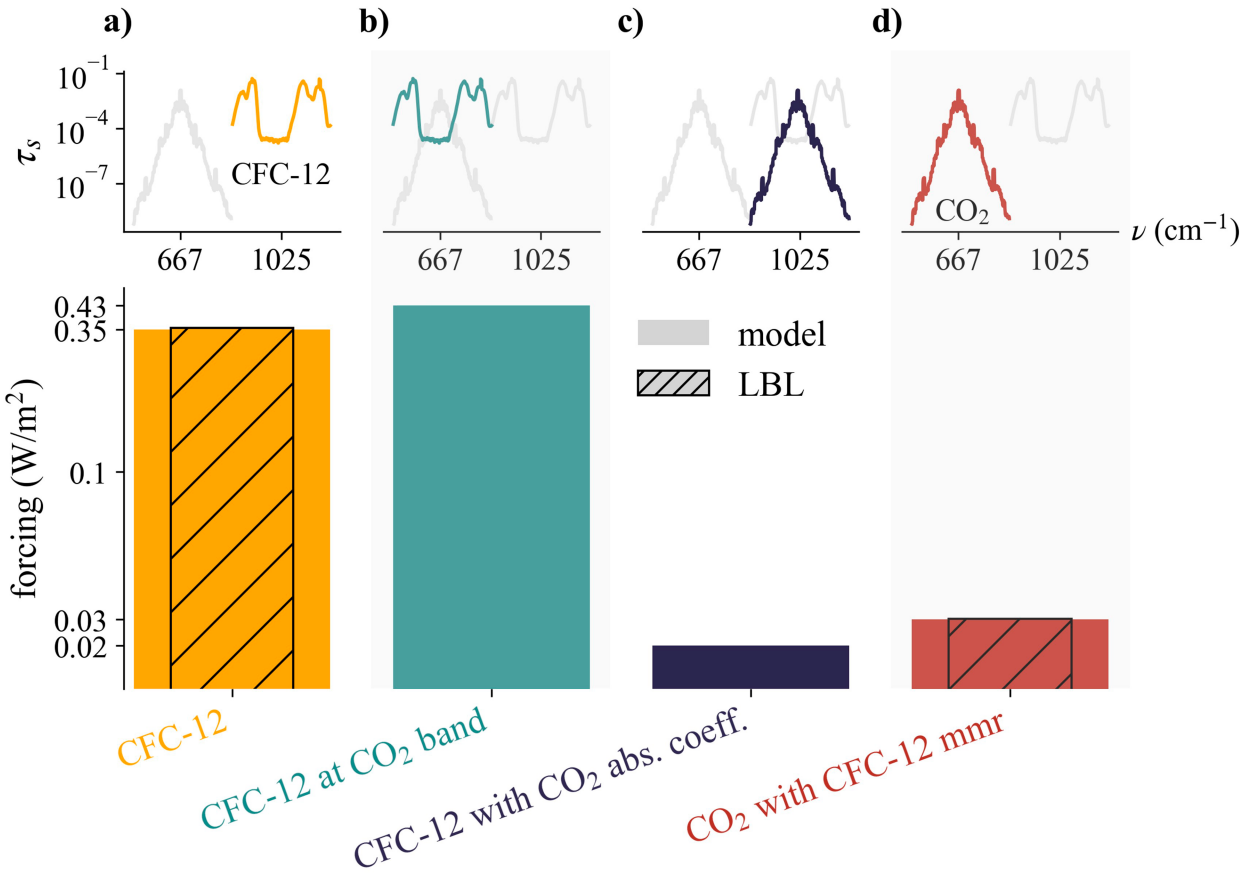

FIG. 5. Forcing resulting from manipulating CFC-12 and optically thin CO_2 (for direct comparison) to illustrate the impact of absorption coefficient magnitude and spectral position on the forcing. (top) The schematics of these manipulations. Optical depth at the surface due to CFC-12 and CO_2, both at present-day CFC-12 concentrations (495 pptv), is shown in gray. The colorful spectra show the changes to the absorption applied to the forcing calculation below. (a) The preindustrial–present-day CFC-12 forcing in a single tropical column (yellow). The black hatching represents the corresponding LBL calculation. (b) The forcing after moving the CFC-12 absorption coefficient to the CO_2 absorption band (teal). (c) The forcing after changing the CFC-12 absorption coefficient mean value to that of CO_2 (navy). (d) The CO_2 forcing at CFC-12 preindustrial and present-day concentrations (red) and the corresponding LBL calculation (hatching).

band-mean absorption coefficient (Fig. 5c) yields a large decrease in the forcing, closer in magnitude to the CO_2 forcing. CFC-12 and CO_2 emit over a comparably sized bandwidth ($\delta_\nu \approx 350$ cm^{-1}), so this factor is not shown. Of course, applying both changes to the Planck function and the absorption coefficient recovers the optically thin CO_2 forcing at 495 pptv (Fig. 5d). This simple exercise illustrates that, as Shine (1991) hypothesized, the larger band-average size (κ^*_{ref}) of the CFC-12 absorption cross section is the main reason for its increased radiative power compared to CO_2 in the optically thin regime.

c. *Atmospheres with water vapor*

Spectral overlap by thicker gases in the atmosphere will reduce the radiative forcing of optically thin constituents. Nitrous oxide, methane, and halocarbons share the longwave spectrum with many gases in different parts of their bands, though here we treat only spectral overlap by water vapor, the strongest greenhouse gas. Our discussion closely follows the approaches outlined in Jeevanjee and Fueglistaler (2020b) and Jeevanjee et al. (2021).

At the wavenumbers where water vapor is optically thick (where $\tau_{H_2O} > \tau^{\text{em}}_{H_2O} \approx 1$), the temperature at the pressure level where H_2O emits replaces T_s in Eq. (9), as the atmosphere will be opaque to thermal radiation below this emission level. To find the water vapor emission temperature, we sort the H_2O optical thickness and split the band into two parts: the part of the band where H_2O is optically thin ($\tau_{H_2O} < \tau^{\text{em}}_{H_2O}$) and a subband where H_2O is optically thick ($\tau_{H_2O} > \tau^{\text{em}}_{H_2O}$). The emission temperature is then found by computationally inverting water vapor's optical thickness for the level where $\tau_{H_2O} \approx \tau^{\text{em}}_{H_2O}$; the details are left to the appendix, section b.

Equation (11) still applies in the portion of the band where H_2O is not emitting. In the subband where H_2O optical thickness is significant, surface temperature is replaced by mean H_2O emission temperature, calculated numerically. The forcing in the two subbands is added together, yielding

$$\mathcal{F}_{i\to f} = [B(T_s, \nu^*) - \overline{B}(\nu^*)]\Delta q\, \tau_s^*\, \delta\nu_{\text{gas}} + [B(T_{\text{em}}^{\text{H}_2\text{O}}, \nu^*) - \overline{B}(T \le T_{\text{em}}^{\text{H}_2\text{O}}, \nu^*)]\Delta q\, \tau_{\text{H}_2\text{O}}^*\, \delta\nu_{\text{H}_2\text{O}}. \quad (12)$$

The first term remains as in Eq. (11): the difference between the surface Planck function and the mean atmospheric Planck function, attenuated by the mean total change in optical depth across the band, but now, it is proportional to the width of the subband that is not covered by H_2O ($\delta\nu_{\text{gas}}$). The second term is analogous to the first, but the Planck function and the unit-concentration optical depth τ^* are evaluated at the temperature and pressure where H_2O emits and scaled by the width of the band where water vapor dominates ($\delta\nu_{\text{H}_2\text{O}}$). This results in a smaller atmospheric contribution $\overline{B}$ and reflects the fact that the optically thin gas is only radiatively active above the water vapor. Note that even when H_2O is optically thick, the thin gas can still exert a forcing, as this second term is not necessarily zero.

d. Application: Radiative forcing by CFC-12

To ensure our theory captures the physics of radiative forcing across a range of surface temperatures, lapse rates, and water vapor concentrations, we compare Eqs. (11) and (12) to line-by-line calculations for the March 1981 monthly mean of ERA5 reanalysis data (Hersbach et al. 2023), chosen for direct comparison to Jeevanjee et al. (2021). Surface temperature and relative humidity for this month are shown in Figs. 6a and 6b. The ERA5 dataset is interpolated onto a standard pressure grid, so the data are processed to exclude pressure levels higher than the surface pressure. The parameters needed to evaluate IRF from Eq. (12) are fit to spectroscopic data from the HITRAN database (Gordon et al. 2017). We note that these fits require a series of choices; while a different approach might yield a different set of absolute parameter values, the physical insights derived from our theory are not sensitive to these values. Our fitting procedure for H_2O and CFC-12 absorption is detailed in the appendix, sections b and c.

Figures 6c–h show the spatial distribution of forcing by present-day concentrations of CFC-12, with our theory on the left and line-by-line calculations on the right. In the upper row, CFC-12 is the only radiatively active species at preindustrial (0 parts per trillion by volume) and present-day (495 pptv) concentrations. Instantaneous radiative forcing closely follows surface temperature and is strongly impacted by topography as there is both less mass above and lower surface temperatures at high-elevation areas such as Antarctica or the Tibetan Plateau. For CFC-12 alone (Figs. 6c–e), the global-mean forcing yielded by our theory is 0.276 and 0.278 W m^{-2} from line-by-line calculations.

Damping of CFC-12 radiative forcing by water vapor is relatively small at about 8% (lower row); we emphasize that, in these calculations, CFC-12 and H_2O are the only radiatively active species. CFC-12 varies from preindustrial to present-day concentrations, while by contrast, water vapor concentrations and temperatures are constant. Note that although water vapor is always more optically thick than CFC-12 by at least an order of magnitude at the surface (Fig. 1b), CFC-12 still exerts a radiative forcing because its optical thickness above the water vapor emission level changes as concentration changes from q_i to q_f.

e. Dependence of forcing on the atmospheric thermal structure

Radiative forcing by all absorbers displays a strong meridional dependency that, in clear skies, can be attributed in varying degrees to surface temperature, atmospheric lapse rates, and water content. The atmospheric-average Planck function $\overline{B}$ in Eq. (11) implies that radiative forcing by optically thin gases depends on the temperature structure of the troposphere. Surface temperature and water vapor concentration have competing effects on the forcing: Warmer temperatures are associated with larger Planck surface emission $B(T_s)$ and so a larger forcing. At the same time, warmer atmospheres can hold more water vapor, which damps the forcing by reducing the Planck emission term from $B(T_s)$ to $B(T_{\text{H}_2\text{O}}^{\text{em}})$.

As surface temperature and lapse rate are highly correlated, we explore the dependence of IRF on only relative humidity and surface temperature. For simplicity, we limit our analysis to optically thin gases in idealized atmospheres with moist adiabatic lapse rates (assuming constant relative humidity) up to an isothermal stratosphere at 200 K (Jeevanjee et al. 2021), calculated using the MetPy Python package (May et al. 2022), to explicitly draw out how forcing depends on temperature and relative humidity.

The Planck function profile can be idealized as a power law in pressure (Koll et al. 2023), where γ describes how the Planck function changes with pressure:

$$B(p) = B(T_s)\left(\frac{p}{p_s}\right)^{\gamma}. \quad (13)$$

The exponent $\gamma = \alpha\gamma_{\text{LR}}$, where $\alpha = [d\ln B(\nu)]/(d\ln T) \approx 4$ in the CFC-12 band (estimated from Fig. 4 in Jeevanjee and Fueglistaler 2020a), and γ_{LR} is a bulk moist adiabatic lapse rate as in Eq. (9) of Koll et al. (2023). Then, the average Planck term $\overline{B}$ can be directly calculated:

$$\overline{B} = \frac{\int_{p_{\text{TOA}}}^{p_s} B(p)dp}{\int_{p_{\text{TOA}}}^{p_s} dp} = \frac{1}{p_s}\int_{p_{\text{TOA}}}^{p_s} B(T_s)\left(\frac{p}{p_s}\right)^{\gamma} dp = \frac{B(T_s)}{1+\gamma}.$$

As the stratosphere is isothermal in this idealized setting, integration to the TOA and the tropopause are equivalent; we integrate to the TOA for mathematical simplicity.

Substitution for $\overline{B}$ in Eq. (11) allows us to write

$$\mathcal{F}_{i\to f} = \left(\frac{\gamma}{1+\gamma}\right)B(T_s, \nu^*)(q_f - q_i)\,\tau_s^*\delta\nu. \quad (14)$$

The presence of water vapor is treated as in Eq. (12), replacing surface emission in the fraction of the band where H_2O is optically thick. As before, this second term is evaluated at

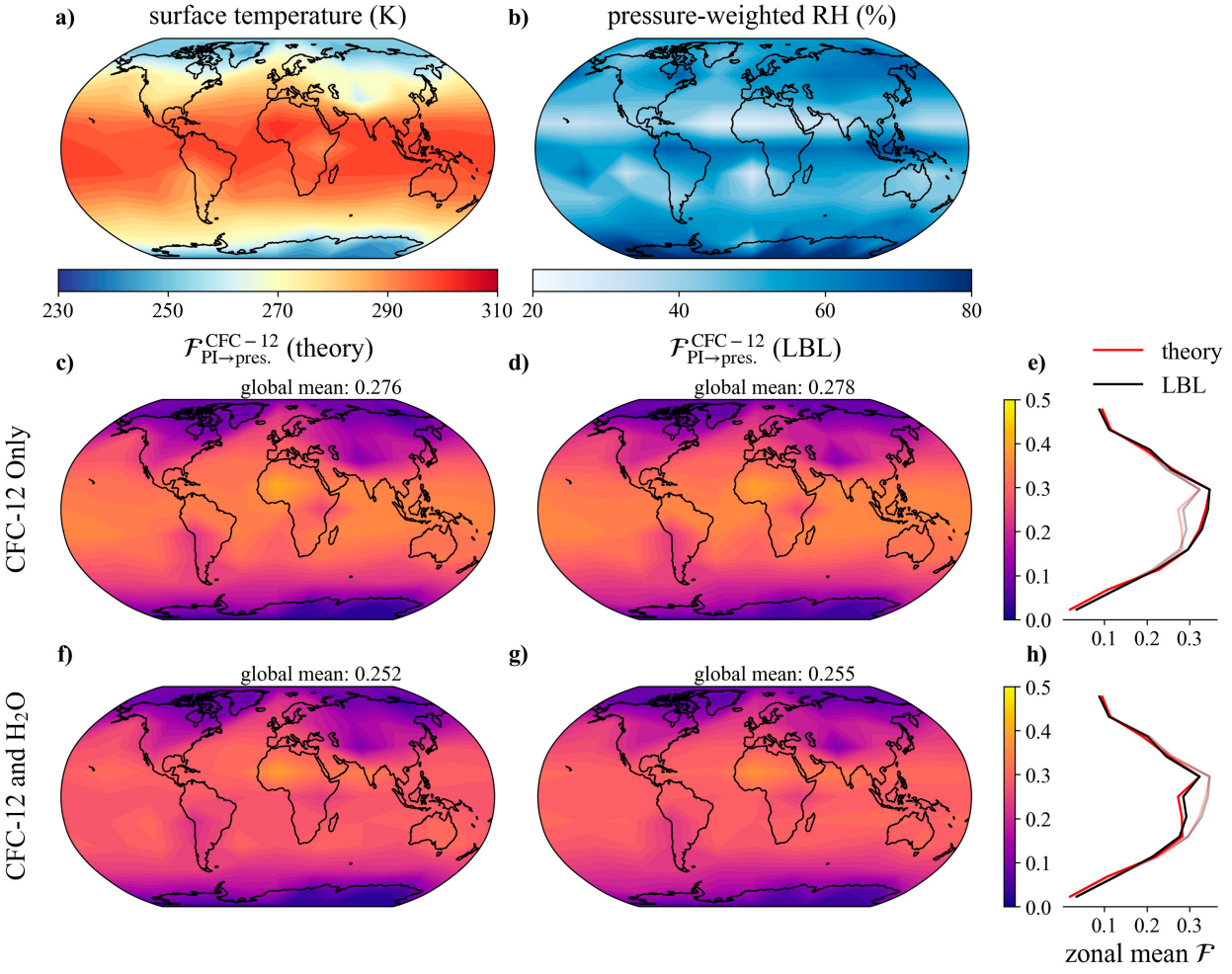

FIG. 6. (a) The surface temperature (K) and (b) pressure-averaged relative humidity in the ERA5 sample used for global calculations. Spectrally integrated preindustrial–present-day CFC-12 forcing is shown in atmospheres (c)–(e) without and (f)–(h) with H_2O overlap. In (c) and (f), the theoretical forcing [Eqs. (11) and (12), respectively] is shown. (d),(g) The corresponding LBL forcing. Zonal means of the model (red) and LBL (black) are shown in (e) and (h); the transparent lines show the zonal means (e) with and (h) without water vapor for direct comparison. Global-mean values for each map are also listed.

water vapor's $\tau = \tau^{\mathrm{em}}$ level, which depends on relative humidity (discussed in the appendix, section b):

$$\mathcal{F}_{i\to f} = \left(\frac{\gamma}{1+\gamma}\right) B(T_s, \nu^*)(q_f - q_i)\,\tau_s^*\,\delta\nu_{\mathrm{gas}} + \left(\frac{\gamma}{1+\gamma}\right) B(T_{\mathrm{em}}^{\mathrm{H_2O}}, \nu^*)(q_f - q_i)\,\tau_{\mathrm{em}}^{*\mathrm{H_2O}}\,\delta\nu_{\mathrm{H_2O}}. \quad (15)$$

Unlike CO_2, whose IRF depends only on the surface and stratospheric temperatures [Eq. (1)], Eqs. (14) and (15) highlight the dependence of thin-gas forcing on tropospheric lapse rate γ. The forcing in moist adiabatic atmospheres can thus be characterized by surface emission attenuated by the total thickening of the atmosphere and scaled by the lapse rate.

Radiative forcing by CFC-12 [Eq. (15)] in atmospheres with idealized moist adiabatic lapse rates is plotted for a range of surface temperatures (260–310 K) and relative humidities in Fig. 7. The idealized power-law bulk lapse rate γ approximates the actual lapse rate with varying faithfulness, resulting in a modeled $\mathcal{F}$ that imperfectly matches LBL calculations and so highlights the sensitivity of the forcing to the temperature structure of the atmosphere. At Earth-like conditions of approximately $20\% < \mathrm{RH} < 80\%$ (e.g., Fig. 6b), CFC-12 forcing magnitude is largely set by surface temperature and attenuation by water vapor is comparatively weak, decreasing the global-mean CFC-12 forcing by only about 8% (Fig. 6), because of CFC-12's spectral position at the edge of the water vapor window. As a point of comparison, CO_2 radiative forcing is decreased by 30% by water vapor overlap in analogous calculations (Jeevanjee et al. 2021) because of the stronger spectral overlap by H_2O absorption lines.

3. Radiative forcing by optically thick gases

a. *Theory*

In the optically thin limit, emission occurs throughout the troposphere and thus can be captured with a linear weighting

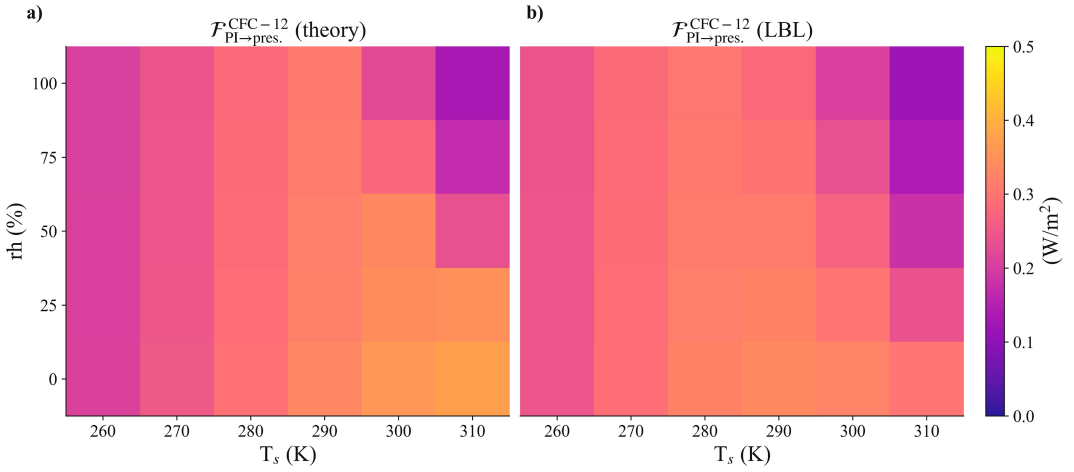

FIG. 7. Comparison of spectrally integrated preindustrial–present-day CFC-12 forcing in atmospheres with idealized moist adiabatic lapse rates across a range of realistic surface temperatures and relative humidities. In (a), the theoretical forcing [Eq. (15)] is shown. (b) The corresponding LBL forcing.

function. Optically thick gases, in contrast, can be thought of as emitting from a single level at each wavenumber. In the broadband, this distinction is drawn when the band-average optical thickness is greater than about 1; then, the emission level is defined at peak absorption. Carbon dioxide is so optically thick that the emission level is in the stratosphere [Eq. (1); Jeevanjee et al. 2021; Wilson and Gea-Banacloche 2012]. Methane and nitrous oxide are also optically thick and therefore can be modeled via an emission-level approximation or Dirac delta weighting function, but inverting line-by-line optical depth for the $\tau \approx 1$ pressure level reveals that this level occurs in the troposphere. We must therefore generalize Eq. (1) to apply it to other gases.

Rather than directly applying the weighting function to monochromatic fluxes and integrating, we adopt the geometric perspective illustrated in Fig. 8a (Wilson and Gea-Banacloche 2012; Jeevanjee et al. 2021; Koll et al. 2023; Stevens and Kluft 2023). When a gas is optically thick, it absorbs longwave radiation at one level and reemits it from a lower pressure and temperature, creating an indent or a "ditch" in the OLR away from the surface blackbody Planck emission (Pierrehumbert 2010). At each wavenumber, the height h of the ditch is the difference between the surface and emission temperatures: $h = B(T_s) - B(T^{\mathrm{em}})$, where $T^{\mathrm{em}} = T[\tau(\kappa, \nu, q) = \tau^{\mathrm{em}}]$ depends on the absorption coefficient value κ and absorber concentration q. The width of the ditch in spectral units, $\delta\nu_s^{\mathrm{em}}(\kappa, q)$, is computed numerically and likewise depends on the details of the absorption coefficient κ and concentration q (Fig. 8). Without restricting spectroscopy, spectrally integrated OLR for such a gas at concentration q can be written as

$$\mathrm{OLR} = \int_\nu B(T_s) - A(T_s, T^{\mathrm{em}}, \delta\nu_s^{\mathrm{em}}),$$

where A indicates the area of the ditch as a function of surface temperature, emission temperature, and emission spectral width for gas concentration q. The exact form of A will depend on the absorption spectrum of the gas. Then generally, the radiative forcing resulting from increasing greenhouse gas abundance from concentration q_i to concentration q_f can be written as

$$\mathcal{F}_{i\to f} = \mathrm{OLR}_i - \mathrm{OLR}_f = A(T_s, T^{\mathrm{em},f}, \delta\nu_s^{\mathrm{em},f}) - A(T_s, T^{\mathrm{em},i}, \delta\nu_s^{\mathrm{em},i}). \quad (16)$$

This is illustrated in Fig. 8, assuming a log-linear triangular absorption coefficient (the appendix, section d) with maximum emission either in the troposphere (Fig. 8a) or the stratosphere (Fig. 8b). The gray curves represent OLR_i and the black curves represent OLR_f, and dependencies on the maximum value (κ_0) and the slope (l) of the absorption coefficient are noted. The OLR at each gas concentration is then the area under the black and gray curves, respectively; the forcing between them is their difference.

Radiative forcing by CO_2 is a special case of Eq. (16) (Fig. 8b). As CO_2 is very optically thick, it emits in the stratosphere, which is close to isothermal: $T^{\mathrm{em},i} = T^{\mathrm{em},f} \approx T_{\mathrm{strat}}$ (Wilson and Gea-Banacloche 2012; Jeevanjee et al. 2021). [Though in practice, this is not always true, adjusting for stratospheric lapse rate makes minimal difference (Seeley 2018).] The height of the absorption ditch is $h = B(T_s) - B(T_{\mathrm{strat}})$; the widths are the stratospheric spectral width $\delta\nu_{\mathrm{strat}}^{\mathrm{em}}$ and the surface spectral width $\delta\nu_s^{\mathrm{em}}$, which may both be calculated by inverting emission optical thickness for wavenumber [Eq. (4) in Jeevanjee et al. 2021]. Because the ditch is a trapezoid due to the assumed flat temperature surface of the stratosphere, spectrally integrated longwave OLR for a given CO_2 concentration can be estimated by computing the area of a trapezoid:

$$\mathrm{OLR} = \int_\nu B(T_s) - \frac{1}{2}[B(T_s) - B(T_{\mathrm{strat}})](\delta\nu_s^{\mathrm{em}} + \delta\nu_{\mathrm{strat}}^{\mathrm{em}}).$$

When CO_2 concentration is changed, the width of the trapezoid is assumed to increase at the surface and in the stratosphere equally and symmetrically by some $\Delta_{i\to f}\nu$, while the height

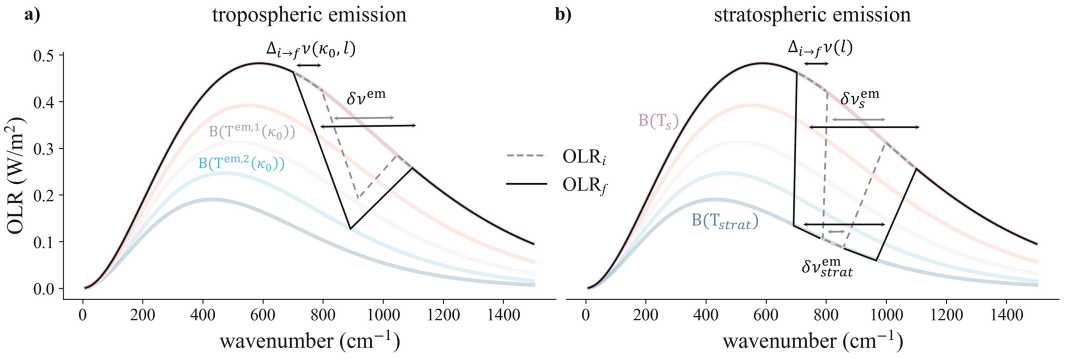

FIG. 8. Schematic illustrating idealized forcing calculation in two cases; the dependence of terms in Eq. (17) on the gas absorption coefficient peak κ_0 and exponentially decaying slope l are noted. Outgoing longwave radiation at initial concentrations (OLR$_i$) is plotted in gray and at increased concentrations in black (OLR$_f$). Planck functions at decreasing temperatures are plotted as contours. (a) A general tropospheric emitter such as N_2O or methane: The gas is optically thick, and so emission temperature depends explicitly on κ_0. Furthermore, spectral width depends on both the slope parameter l and κ_0. (b) The CO_2 case: The gas is very optically thick and emits at a constant stratospheric temperature at both concentrations q_i and q_f. In this case, emission temperature depends on the absorption coefficient peak κ_0 only insofar as it is large enough to ensure stratospheric emission, and the equal emission temperature at both concentrations ensures that $\Delta\nu$ depends only on the slope parameter l. In either case, radiative forcing will be a function of the difference between the area of the black indent and the gray indent.

remains constant (Fig. 8b). Then, the forcing is the difference in the areas of the two trapezoids:

$$\mathcal{F}_{i\to f} = [B(T_s) - B(T_{\mathrm{strat}})]\Delta_{i\to f}\nu.$$

This is equivalent to Eq. (1), where $\Delta_{i\to f}\nu = 2l[\ln(q_f) - \ln(q_i)]$ can be derived by inverting the optical depth for the optically thick wavenumbers in Eq. (10) (Wilson and Gea-Banacloche 2012; Jeevanjee et al. 2021).

Gases such as N_2O or CH_4 are not as optically thick as CO_2 and emit in the troposphere, so that their emission temperature changes with gas concentration (Fig. 8a). Assuming piecewise-exponential absorption coefficients, gases with tropospheric emission can be understood as a special case of Eq. (16):

$$\mathcal{F}_{i\to f} = \frac{1}{2}[B(T_s) - B(T^{\mathrm{em},f})]\delta\nu_s^{\mathrm{em},f} - \frac{1}{2}[B(T_s) - B(T^{\mathrm{em},i})]\delta\nu_s^{\mathrm{em},i}. \quad (17)$$

To treat overlap with H_2O, the optical depth of water vapor is numerically inverted for emission temperature at each wavenumber and the mean across the band is calculated (Jeevanjee et al. 2021; see the appendix, section b). Then, H_2O emission temperature replaces surface emission in Eq. (17), and spectral width is calculated at the water vapor emission surface:

$$\mathcal{F}_{i\to f} = \frac{1}{2}[B(T_{\mathrm{em}}^{\mathrm{H_2O}}) - B(T^{\mathrm{em},f})]\delta\nu_{\mathrm{H_2O}}^{\mathrm{em},f} - \frac{1}{2}[B(T_{\mathrm{em}}^{\mathrm{H_2O}}) - B(T^{\mathrm{em},i})]\delta\nu_{\mathrm{H_2O}}^{\mathrm{em},i}. \quad (18)$$

b. Application: Methane

As with other greenhouse gases, methane has become more abundant since preindustrial times (Forster et al. 2021). Global-mean preindustrial–present-day radiative forcing due to methane is about 0.6 W m^{-2} (Forster et al. 2021). We next construct a simple model of methane forcing.

The absorption coefficient of methane is quite irregular across its band, so for simplicity, we sort and then split it into two subbands: one optically thick and one optically thin (see the appendix, section e for details). Adding Eqs. (11) and (17) yields the total forcing exerted by methane across these two bands:

$$\mathcal{F}_{i\to f} = [B(T_s) - \overline{B}](q_f - q_i)\tau_s^*\,\delta\nu + [B(T_s) - B(T^{\mathrm{em},f})] \times \frac{\delta\nu_s^{\mathrm{em},f}}{2} - [B(T_s) - B(T^{\mathrm{em},i})]\frac{\delta\nu_s^{\mathrm{em},i}}{2}. \quad (19)$$

As before, for atmospheres including water vapor, the H_2O emission temperature $T_{\mathrm{H_2O}}^{\mathrm{em}}$ is determined numerically and replaces the surface temperature. Similarly, $\delta\nu^{\mathrm{em}}$ and τ^* are evaluated at the H_2O emission pressure rather than the surface:

$$\mathcal{F}_{i\to f} = [B(T_{\mathrm{H_2O}}) - \overline{B}](q_f - q_i)\tau_{\mathrm{H_2O}}^*\,\delta\nu + [B(T_{\mathrm{H_2O}}) - B(T^{\mathrm{em},f})] \times \frac{\delta\nu_{\mathrm{H_2O}}^{\mathrm{em},f}}{2} - [B(T_{\mathrm{H_2O}}) - B(T^{\mathrm{em},i})]\frac{\delta\nu_{\mathrm{H_2O}}^{\mathrm{em},i}}{2}. \quad (20)$$

Equations (19) and (20) compare well against LBL calculations across a range of relative humidity and temperature structures from a sample of ERA5 (Figs. 6a,b). Because the band split and absorption coefficient idealizations are somewhat local in concentration, we show preindustrial–present-day methane forcing (Figs. 9a–f) and present-day to 4× present-day concentrations (Figs. 9g–l). Though the methane absorption coefficient is irregular and disjoint parts of the methane band emit in different ways, treating the band as a combination of optically

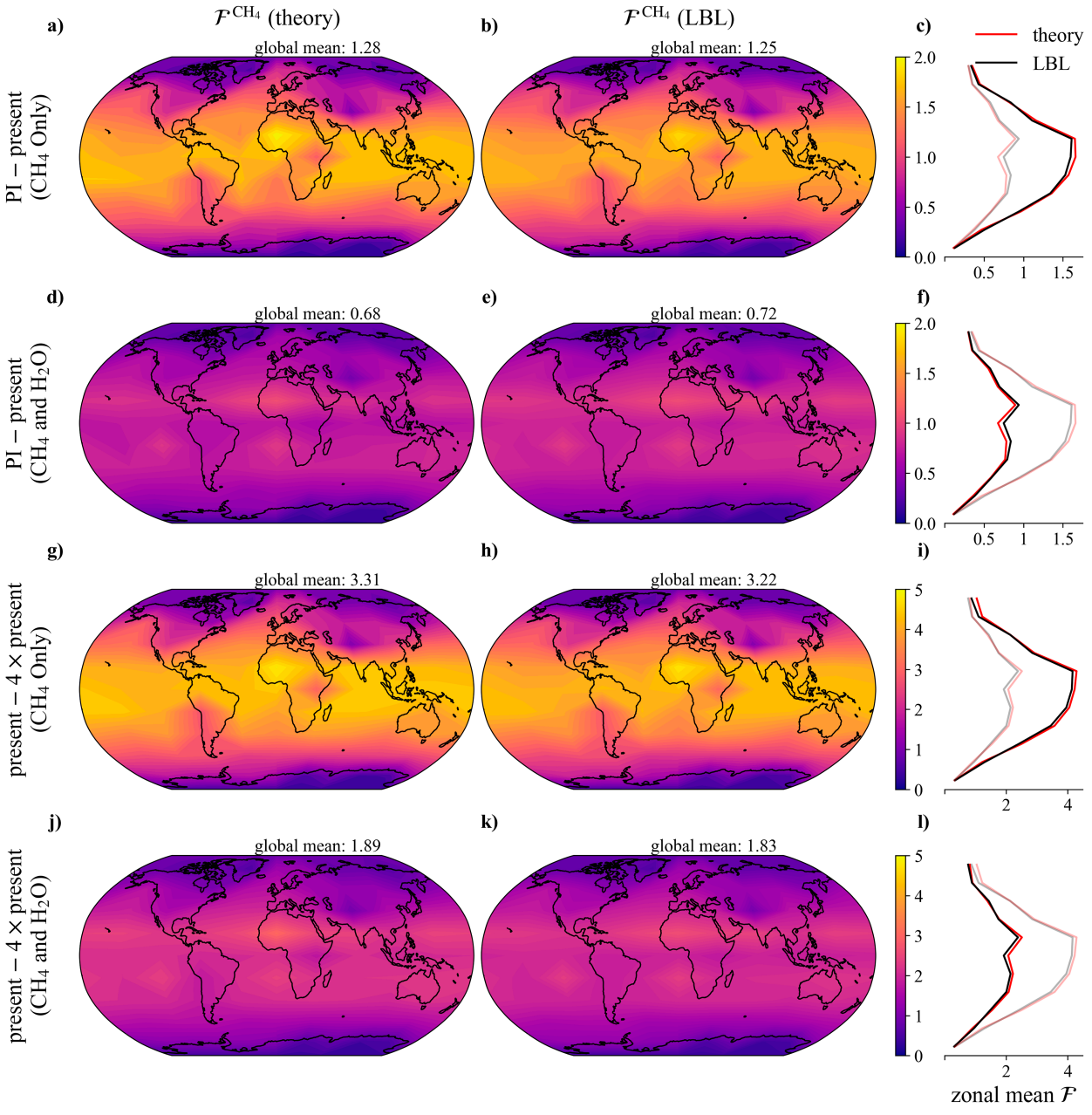

FIG. 9. Theoretical methane forcing calculated via Eqs. (19) and (20) and corresponding LBL calculations from (a)–(f) preindustrial to present-day and (g)–(l) present–4× present-day concentrations in ERA5. (a)–(c) Modeled, LBL, and zonal-mean radiative forcing from preindustrial to present-day concentrations in a methane-only world. (d)–(f) The spectral overlap with H_2O. (g)–(i) The present-day to a quadrupling of present-day methane concentrations in methane-only ERA5. (j)–(l) The forcing due to a quadrupling of methane concentrations including water vapor overlap. As in Fig. 6, the transparent lines on (e),(i) and (f),(l) show the zonal means with and without water vapor for direct comparison.

thick and optically thin behaviors captures total forcing well across these different concentrations. Methane IRF is attenuated by water vapor overlap by almost 50%, more than CFC-12 (~8%) and CO_2 (~30%) due to the stronger overlap with water vapor lines (Fig. 1d). As with CFC-12, Earth's surface topography is visible in the forcing maps due to its effect on the surface temperature and atmospheric mass, with smaller forcing over high-elevation areas.

The presence of water vapor adds an additional challenge for gases emitting in the troposphere, as not only the surface value but also the entire profile of the modeled CH_4 optical depth must be correct. Nonetheless, deviations of model values away

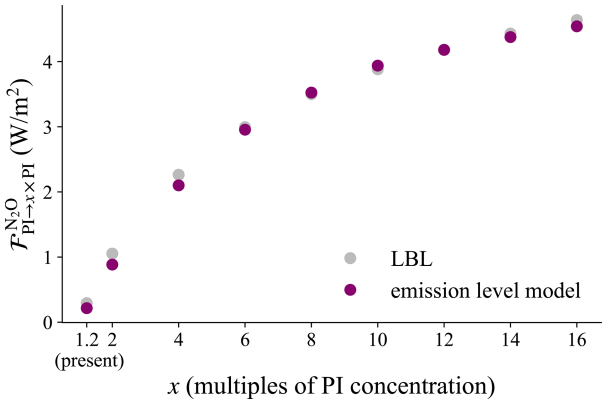

FIG. 10. Theoretical radiative forcing by N_2O in its υ_1 band (centered at 1284 cm^{-1}) for concentrations of N_2O away from preindustrial (purple) is compared to LBL calculations (gray).

from reference calculations in atmospheres with water vapor are small in magnitude, and the theory captures attenuation by water vapor across a variety of temperature and relative humidity conditions well. Overall, treating methane as a combination of thick and thin regimes yields good agreement with line-by-line calculations. In calculations sampling the global range of conditions, however sparsely, radiative forcing by methane is modeled as depending on the square root of concentration rather than the logarithm (Etminan et al. 2016; Byrne and Goldblatt 2014; Forster et al. 2021). Recognizing that methane forcing consists of both optically thick and optically thin spectral regions suggests that the square root dependence on concentration arises from a combination of linear and logarithmic regimes.

c. *Application: N_2O*

Nitrous oxide has three significant bands at present-day concentrations (Figs. 1e and 11a). As the absorption coefficients in each band are approximately log-linear triangles and vary in optical thickness in different ways, N_2O provides an ideal testbed for our discretization of gases into thin and thick regimes. We apply Eq. (17) to N_2O's first vibrational mode υ_1 (1220–1340 cm^{-1}); line-by-line calculations reveal that this band is optically thick at preindustrial concentrations and begins to emit in the stratosphere at 10 times preindustrial concentrations, thus spanning values of T^{em}. We idealize υ_1 N_2O absorption with a piecewise-exponential function, invert the resulting optical thickness profile for the temperature and pressure where $\tau \approx 1$ (see the appendix, section f), and solve for IRF using Eq. (17) across this wide range of concentrations. Figure 10 shows good agreement of the theory with line-by-line calculations in this band. Small errors stem from the fact that as concentration rises, new parts of the absorption coefficient that are not quite constant in slope are revealed. The functional form of the forcing with concentration is almost perfectly logarithmic, an observation we extend to the rest of the N_2O spectrum next.

N_2O's surface optical thickness at preindustrial concentrations (270 ppbv) is illustrated in Fig. 11a. The υ_2 and $2\upsilon_2$ bands are optically thin, with $\tau_s < \tau^{em}$ across their bands, though this classification will change as gas concentration increases. As building analytical models for the υ_2 and $2\upsilon_2$ bands would entail a similar procedure as that of the υ_1 band, we omit it here. Rather, we turn to line-by-line calculations to understand how the three bands work together to exert a forcing with a square root relationship to concentration. We posit that N_2O forcing can be understood by treating each band independently. Then, the optically thin bands will contribute a linear increase in forcing for each increase in gas concentration, and optically thick bands will yield a logarithmic contribution. The total forcing will then be the sum of linear and logarithmic terms.

We use line-by-line computations to test this idea (Fig. 11b). Concentrations of N_2O are increased from preindustrial by the given multiple, and the forcing contributed by each of the bands is shown. Linear and logarithmic functional forms fit the optically thin and optically thick line-by-line calculations in Fig. 11b remarkably well. Thus, the total functional form of N_2O forcing

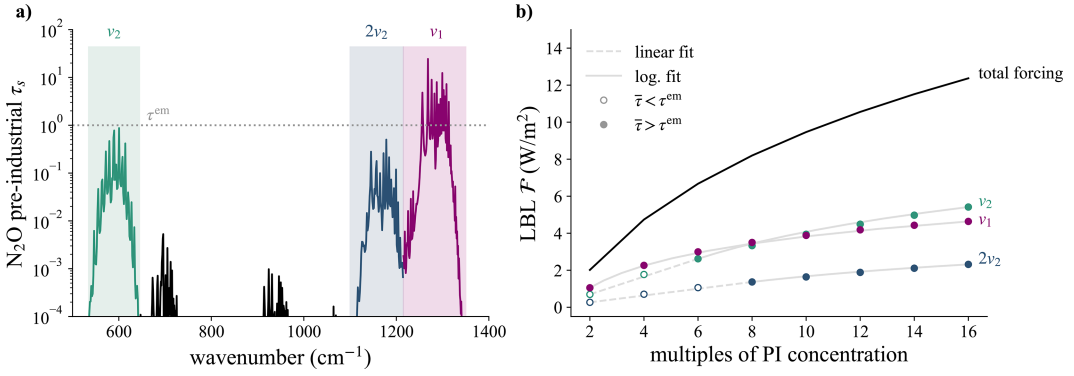

FIG. 11. Extension of the thin and thick gas forcing theory to N_2O, which exhibits both properties across the longwave spectrum. (a) The surface optical depth at preindustrial N_2O concentrations. N_2O is split into three radiatively active bands (teal, blue, and purple). (b) The LBL forcing contribution by each of these bands in corresponding colors. When the band-mean optical thickness is less than the emission optical thickness, the forcing is plotted in empty circles and a linear fit is shown in dashed gray. When the band is emitting largely from the atmosphere, the forcing is plotted in filled circles and a logarithmic fit is shown in solid gray.

with concentration can be understood as shaped by linear and logarithmic contributions from optically thin and optically thick bands. This supports the idea that much as carbon dioxide's logarithmic scaling originates from its absorption coefficient distribution rather than the behavior of individual absorption lines, the empirical square root functional form that has been fit to N_2O (e.g., Byrne and Goldblatt 2014) stems from its bands acting in different opacity regimes.

While N_2O overlaps spectrally with other gases, most significantly CH_4 and H_2O (Fig. 1), we do not study this overlap here. Spectral overlap by CH_4 could be included similarly as that by H_2O: by replacing surface emission with the emission of the $\tau_{CH_4} \approx 1$ surface. Line-by-line calculations with and without CH_4 (not shown) reveal that spectral overlap of N_2O by preindustrial concentrations of CH_4 attenuates the forcing by a multiplicative factor of about 1.1 across the concentrations shown in Fig. 11 but does not change any of the insights discussed above.

4. Summary and discussion

In summary, we have taken an analytical approach to gain insight into radiative forcing by greenhouse gases across opacity regimes. In the optically thin limit, two key assumptions simplify Schwarzschild's equations: 1) atmospheric Planck emission can be replaced with the pressure-averaged Planck emission and 2) when the change in optical depth is small, it is approximately equal to the change in transmissivity. These insights apply both monochromatically and in the broad band; to facilitate the latter calculation, spectroscopy is simplified with the mean value of the absorption coefficient across its band. Optically thin gases including CFC-11 and CFC-12 and optically thin CO_2 emit in this vertically and spectrally averaged way, and thus, a linear increase in thin gas concentration yields a linear increase in radiative forcing. Though we focus on only well-mixed gases, this is true of any optically thin atmospheric constituent as long as its total surface optical thickness τ_s is linear in its concentration, since τ_s does not depend on the distribution of the gas in the column. (An exception to the generality of our theory is the water vapor continuum because its optical thickness does not depend linearly on its concentration.) Our theory has identified that the most important contributor to CFC-12's powerful radiative forcing is the large average size of its cross section. Finally, we examined the relationship of radiative forcing to atmospheric temperature profiles, finding that optically thin gases are sensitive to the details of the thermal profile of the troposphere.

Next, we bridged our understanding of optically thin gas forcing with existing work on optically thick CO_2 forcing to study gases that emit in the troposphere. Methane presented unique challenges due to the irregularity of its spectrum. We sorted the absorption coefficient along the wavenumber axis and then split it into optically thin and optically thick regimes. Combining the thin and thick approaches yielded good results at preindustrial, present-day, and 4 times present-day concentrations.

Finally, nitrous oxide has three radiatively active bands at Earth-like concentrations that are each classified as optically thick or optically thin. Idealizing one optically thick band with piecewise-triangular spectroscopy and tropospheric emission to space yielded good agreement with line-by-line results across a range of concentrations. Even though this υ_1 band breaks several of the requirements outlined in Romps et al. (2022) and Seeley (2018)—including an exponential and symmetrical absorption coefficient and an unchanging emission temperature with concentration—its radiative forcing is remarkably logarithmic in concentration. The accuracy of this band model along with our methane model supports the physical insights underlying the CO_2 ditch model and the theory that CO_2 is logarithmic in concentration due to the shape of its absorption coefficient, as these ideas generalize to other gases with similar key properties [here, optical thickness and piecewise-exponential absorption coefficients; the theory does not generalize to water vapor because the relationship of its concentration to emission temperature is highly complex, e.g., Eq. (A2)]. By treating thin and thick bands independently, we demonstrated that optically thin bands contribute a linear increase in forcing with concentration, while optically thick bands contribute an increase in forcing that is, to first order, logarithmic. Thus, we categorized all of Earth's major well-mixed greenhouse gases into optically thin and optically thick bands. While this is a great simplification of optical thickness, which is a continuous and not a binary quality, the linear combinations of these two regimes reproduce the total behavior of these gases well.

Our analytical work aims to derive understanding of the relationship between radiative forcing and the optical thickness of well-mixed gases, and accordingly, we make many simplifications with the goal of analytical tractability rather than prediction or accuracy. One such simplification is performing our analysis only in single atmospheric columns, following prior work (Romps et al. 2022; Jeevanjee et al. 2021). Conversely, functional forms studied for the sake of prediction in IPCC reports and related studies are typically empirically fit global means over time, accounting for clouds, seasonally variable temperature distributions, spectral overlap by various gases, and fast adjustments (Byrne and Goldblatt 2014; Hansen et al. 1988; Forster et al. 2021; Huang et al. 2016). Though our values of forcing cannot be directly compared to these global averages, our approach sheds some light on the spectroscopic contribution of each gas to its radiative response, and related work has shown that implications of theories derived in single columns can hold for more complicated global calculations (e.g., Zhang et al. 2020). The similarity of our results to more complete calculations including spectral overlap by other gases, clouds, and stratospheric adjustments further supports the generality of our theory (Chiodo and Polvani 2022), and the dependence of optically thin gas IRF on the temperature structure of the troposphere supports the idea that ozone depleting substances may have a particularly strong lapse-rate feedback (Liang et al. 2022). Nonetheless, in the future, a rigorous assessment of the relationship of these single-column calculations to global forcing and feedback experiments should be performed.

Acknowledgments. We are grateful to three anonymous reviewers and the editor for their helpful feedback. We additionally thank Nadir Jeevanjee, Andrew Williams, Tim

Cronin, and Alex Parsells for insightful discussions about this work. Finally, we acknowledge the Earth Observation Data Group's fantastic website on the spectral optical thickness of atmospheric gases (https://eodg.atm.ox.ac.uk/ATLAS/zenith-absorption), which was a frequent reference and inspired Fig. 1. This work was supported by the U.S. National Science Foundation (Award AGS 19-16908) and the National Oceanic and Atmospheric Administration (Award NA200AR4310375). The authors report no conflicts of interest.

Data availability statement. All Python functions used for modeling as well as figure production are available in the Jupyter notebook at https://doi.org/10.5281/zenodo.15214618. ERA5 data are freely available at the Climate Data Store.

APPENDIX

Idealized Absorption

a. Emission optical depth

The emission optical thickness τ^{em}, or the optical thickness at which atmospheric emission outweighs surface emission, is modeled throughout the paper via

$$\tau^{\text{em}} = [\tilde{\Gamma}(1+\gamma)]^{1/\gamma}, \tag{A1}$$

where $\gamma = (d\ln B)/(d\ln\tau) = (\alpha/\beta)[(R_d\Gamma)/g]$ and $\tilde{\Gamma}$ is the Euler gamma function (Jeevanjee et al. 2021; Jeevanjee and Fueglistaler 2020a). The exponent β sets the average slope of the optical thickness profile, Γ is the local (tropospheric or stratospheric) lapse rate at the emission level, $R_d = 287$ J kg^{-1} K is the ideal dry gas constant, and $g = 9.8$ m s^{-2} is the acceleration due to gravity. The coefficient $\alpha = [d\ln B(\nu)]/(d\ln T)$ and captures the relationships between the Planck function, temperature, and wavenumber for a given gas band. Equation (A1) is derived by inverting the outgoing longwave radiation of an idealized gas for τ^{em} and as such depends on Planck function, which varies spectrally; the temperature dependence is smaller and so ignored. For a more detailed discussion, see appendix B of Jeevanjee et al. (2021). To first order, $\tau^{\text{em}} \approx 1$ as predicted by the cooling-to-space theory or the $\tau = 1$ law (e.g., Pierrehumbert 2010).

b. H_2O

Water vapor optical depth is the sum of H_2O line absorption and continuum absorption, each of which depends on relative humidity and temperature in different ways. Where both line and continuum absorption act, the optical thickness of water vapor is given by Eq. (12) in Jeevanjee and Fueglistaler (2020a) and Eq. (11a) in Jeevanjee et al. (2021):

$$\begin{aligned}\tau_{\text{H}_2\text{O}} &= \tau^{\text{line}}_{\text{H}_2\text{O}} + \tau^{\text{cont}}_{\text{H}_2\text{O}} \\ &= D\kappa^{\text{line}}_{\text{ref}}\frac{p}{p^{\text{line}}_{\text{ref}}}\text{WVP}_0 e^{-(L/R_v)T} + D\frac{\text{RH}^2\rho^*_v(T^{\text{cont}}_{\text{ref}})\kappa^{\text{cont}}_{\text{ref}}}{\text{RH}^{\text{cont}}_{\text{ref}}\Gamma\alpha}e^{\alpha(T-T^{\text{cont}}_{\text{ref}})}.\end{aligned} \tag{A2}$$

Here, $\tau^{\text{line}}_{\text{H}_2\text{O}}$ and $\tau^{\text{cont}}_{\text{H}_2\text{O}}$ are the optical thickness of water vapor due to line and continuum absorption, respectively; $\kappa^{\text{line}}_{\text{ref}}$ and $\kappa^{\text{cont}}_{\text{ref}}$ are the reference line and continuum absorption coefficients, respectively; $p^{\text{line}}_{\text{ref}}$ and $\text{RH}^{\text{cont}}_{\text{ref}}$ are the pressure and relative humidity at which the reference absorption coefficients are sampled, respectively; WVP_0 is the reference water vapor path;

TABLE A1. Descriptions of parameters needed for calculating optical thickness by water vapor.

Parameter	Description	Value	Source
$\tau^{\text{em,CFC-12}}$	Emission τ (CFC-12 overlap)	0.6	Eq. (A1)
$\tau^{\text{em,CH}_4}$	Emission τ (CH_4 overlap)	0.7	Eq. (A1)
$\kappa^{\text{line, CFC-12}}_{\text{ref}} = \kappa_0 e^{-(\lvert\nu_0-\nu\rvert)/l}$	Reference H_2O line coefficient (CFC-12 overlap)	$\kappa_0 = 0.6$ m^2 kg^{-1} $\nu_0 = 1200$ cm^{-1} $l = 7$ cm^{-1}	Fit to LBL
$\kappa^{\text{line,CH}_4}_{\text{ref}} = \kappa_0 e^{-(\lvert\nu_0-\nu\rvert)/l}$	Reference H_2O line coefficient (CH_4 overlap)	$\kappa_0 = 3.8$ m^2 kg^{-1} $\nu_0 = 1450$ cm^{-1} $l = 35$ cm^{-1}	Fit to LBL
$p^{\text{line}}_{\text{ref}}$	Reference line absorption pressure	370 hPa	Jeevanjee and Fueglistaler (2020b)
$\text{WVP}_0 = \frac{T_{av}\text{RH}p^\infty_v}{\Gamma L}$	Reference water vapor path	T_{av} = average temperature (K) RH = relative humidity (%) Γ = lapse rate (K m^{-1})	Jeevanjee and Fueglistaler (2020b)
L	Specific heat of vaporization of water	2.5×10^6 J kg^{-1}	Jeevanjee and Fueglistaler (2020b)
p^∞_v	Reference value for saturation vapor pressure	2.5×10^{11} Pa	Jeevanjee and Fueglistaler (2020b)
R_v	Gas constant for water vapor	461 J (kg K)$^{-1}$	Jeevanjee and Fueglistaler (2020b)
$\kappa^{\text{cont}}_{\text{ref}}$	Mean reference H_2O self-continuum coefficient	0.006 m^2 kg^{-1}	Line-by-line model
$T^{\text{cont}}_{\text{ref}}$	Continuum reference temperature	275 K	Jeevanjee et al. (2021)
$\text{RH}^{\text{cont}}_{\text{ref}}$	Continuum reference RH	0.75	Jeevanjee et al. (2021)
ρ^*_v	Saturation vapor density	kg m^{-2}	Jeevanjee et al. (2021)
$\alpha = 2\frac{L}{R_v T^2_{\text{ref}}} - \sigma$	Vapor pressure scaling	$\sigma = 0.02$ K^{-1}	Jeevanjee et al. (2021)

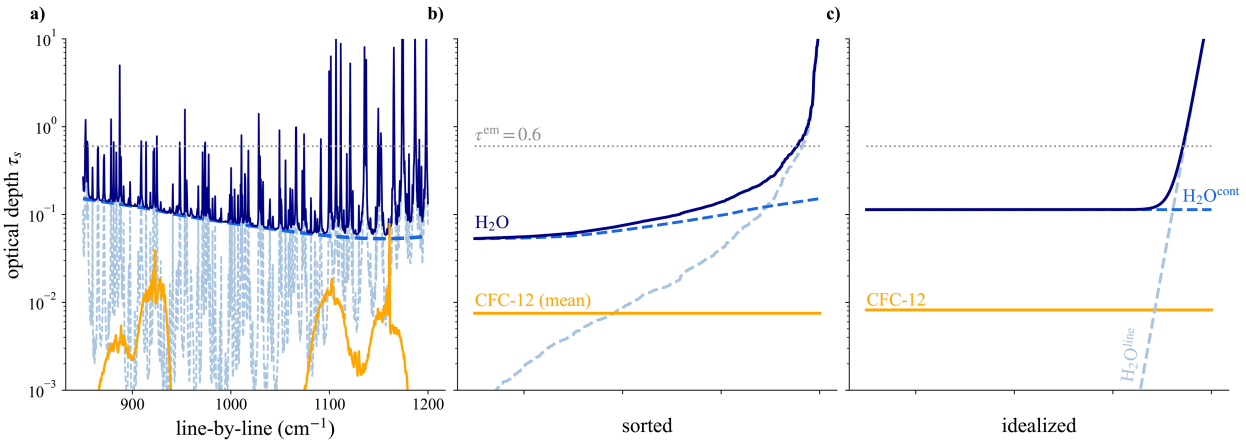

FIG. A1. A schematic illustrating the idealization of the CFC-12 absorption coefficient and its spectral overlap with H_2O. Orange represents CFC-12, dashed light blue represents H_2O line absorption, dashed medium blue represents H_2O self-continuum absorption, and navy blue represents their sum. The emission optical depth $\tau^{em} = 0.6$ line is drawn in gray on each plot. (a) The LBL surface optical depth; (b) the H_2O absorption coefficients are sorted and the CFC-12 mean value is shown. (c) Absorption coefficients are idealized: $\kappa_{CFC\text{-}12}$ and $\kappa^{cont}_{H_2O}$ are parameterized as lines, and $\kappa^{line}_{H_2O}$ falls off exponentially from its peak value. The resulting optical depths are computed according to Eq. (A2) for H_2O and Eq. (10) for CFC-12.

L is the specific heat of vaporization of water; R_v is the gas constant for water vapor; ρ^*_v is the saturation vapor density; Γ is the lapse rate; and α is the vapor pressure scaling. Specific constants and coefficient fits are recorded in Table A1. We consider continuum absorption only in the atmospheric window and disregard foreign continuum absorption as it is small here.

Next, we wish to invert Eq. (A2) for the emission temperature, finding T where $\tau_{H_2O}(T) = \tau^{em}_{H_2O}$; this temperature will replace surface temperature where water vapor is optically thick. Unfortunately, Eq. (A2) cannot be solved directly for $T(\tau = \tau^{em})$. Furthermore, H_2O does not always overlap the entire optically thin gas band (see Fig. A1a). The magnitude and extent of this overlap depend on temperature and relative humidity. Thus, we must determine 1) how much of the optically thin gas band is covered by optically thick water vapor and 2) the average emission temperature of the water vapor in the overlapping part of the band. To invert Eq. (A2) for water vapor emission temperature, we assume no correlation between the band-average absorption coefficient of the optically thin forcer and H_2O. Then, we can sort the H_2O absorption coefficient and numerically solve for emission temperature in the portion of the band where H_2O is optically thick.

In the optically thick case, the shape of the greenhouse gas absorption coefficient matters and we cannot make the noncorrelation assumption. In this case, Eq. (A2) is solved numerically and monochromatically across the band for T^{em}. The band-average T^{em} then replaces surface temperature in our model equations, as in Jeevanjee et al. (2021).

c. CFC-12

As CFC-12 is optically thin, we use a band-average absorption coefficient of 198 m^2 kg^{-1}. Next, we add in spectral overlap by water vapor as described by Eq. (12). The line-by-line absorption coefficients are detailed and highly variable (Fig. A1a). Assuming that the H_2O absorption coefficient is uncorrelated with the CFC-12 coefficient allows us to sort the H_2O overlap along the wavenumber axis (Fig. A1b). Fitting exponential and linear functions to the line and continuum absorption coefficients, respectively, yields good agreement in optical thickness profile to line-by-line coefficients (Fig. A1c). Exact values are listed in Table A2.

d. Idealized absorption coefficients

Here, we discuss the details of the absorption coefficient idealizations for CFC-12, N_2O, and methane, and water vapor overlaps, where applicable. Absorption coefficients are generally assumed to be band-averaged, constant values for optically thin gases and exponentially triangular for optically thick gases, with the functional form

$$\kappa = \kappa_0 e^{-(|\nu_0 - \nu|)/l}. \tag{A3}$$

Here, κ_0 gives the height, or the peak, of the triangle and l gives the slope of the exponential falloff. The spectral coordinate of κ_0 is given by central wavenumber ν_0. Parameter values for each gas are explicitly recorded in tables below.

We note that each absorption coefficient fit requires a set of choices, the combination of which affects the accuracy of the theory (see also Koll et al. 2023; Jeevanjee and Fueglistaler 2020a; Jeevanjee et al. 2021). We fit each parameter of the absorption coefficient separately where possible to understand

TABLE A2. Descriptions of parameters needed to model radiative forcing by CFC-12.

Parameter	Description	Value	Source
ν^*	CFC-12 band center	1025 cm^{-1}	LBL model
$\delta\nu$	Width of CFC-12 band	350 cm^{-1}	LBL model
κ^*_{ref}	Mean absorption coefficient	198 m^2 kg^{-1}	LBL model

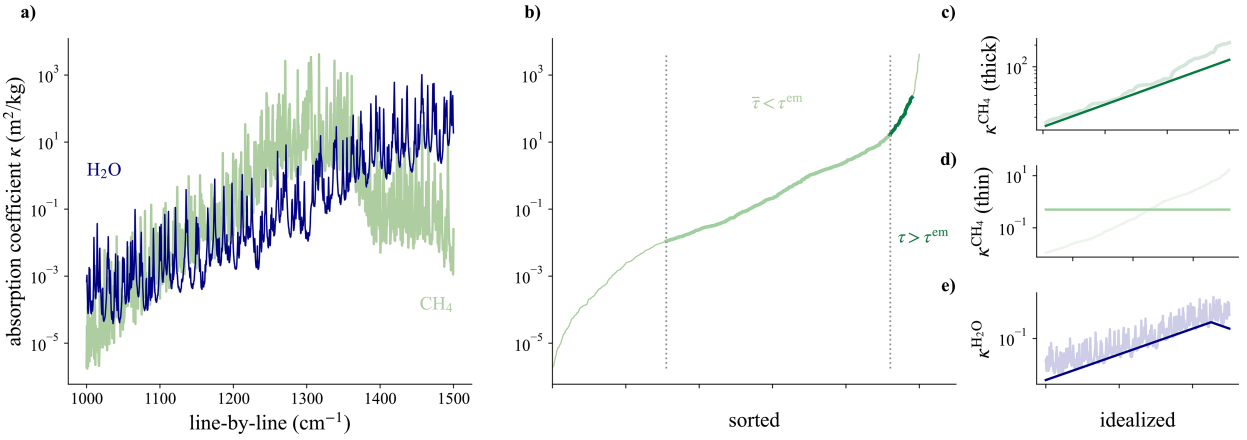

FIG. A2. A schematic illustrating the idealizations to methane and H_2O spectroscopy. Green represents CH_4, and blue shows line absorption by H_2O. (a) The LBL mass absorption coefficients in the 1000–1500 cm^{-1} band. (b) The sorted CH_4 absorption coefficient; in practice, H_2O is sorted by the same index, though this is not shown. This absorption coefficient is split into an optically thin band, defined as where mean optical thickness is less than the emission optical depth ($\overline{\tau} < \tau^{em}$, light green) and an optically thick one ($\tau > \tau^{em}$; dark green). (c) The exponential fit to the thick part of the sorted absorption coefficient. (d) The mean value absorption coefficient approximation for the part of the band where the mean τ is always optically thin. (e) The model for line absorption by water vapor, taken from Eq. (10) in Jeevanjee and Fueglistaler (2020b).

where any errors arise. While a different fitting approach may result in different values of κ_0, l, and ν_0, the physical insights gained from the model remain unchanged. Fitting methodically ensures that the idealized absorption coefficients are parameterizing the real absorption coefficient in physically tractable ways, as in practice there are many values of κ_0 and l that could successfully recreate gas behavior.

e. CH_4

The methane spectrum is not as well behaved as that of other gases, with small adjacent sections that differ in magnitude, slope, and optical thickness (Fig. A2a). To address this, we apply insight from our treatment of water vapor to assume the methane absorption coefficient is uncorrelated with Planck function across its band. This allows us to sort the methane absorption coefficient by magnitude along the wavenumber axis (Fig. A2b). This assumption is not dissimilar from that made in correlated-k distributions, where absorption coefficients are similarly sorted across wavenumber bands for easier spectral integration (e.g., Fu and Liou 1992). Then, we split the coefficient into two radiatively active bands: one where the mean optical depth at the surface is always smaller than the methane emission optical depth [$\tau^{em}_{CH_4} \approx 0.82$ according to Eq. (A1)] across a range of concentrations (Fig. A2b, light green) and one where the whole band is emitting in the atmosphere (Fig. A2b, dark green). The very optically thin leftmost part of the band is ignored as it does not exert a forcing. The very large rightmost part of the band is also disregarded; this tail is small (about 10 cm^{-1}), and as it emits in the stratosphere where lapse rates are small, it does not exert a forcing. The natural split between the two bands is the elbow in slope, though in practice, the boundary between these two bands is fluid as concentration changes, so this choice is somewhat local to present-day concentrations.

The optically thick absorption coefficient is simplified with an exponential function [Eq. (A3)], with $\kappa_0 = 125$ m^2 kg^{-1}, $l = 14$ cm^{-1}, and ν_0 being the end of the band (Fig. A2c; Table A3). As with N_2O, the slope parameter l is isolated by optimizing model forcing to line-by-line calculations in an idealized isothermal atmosphere with discontinuous, varying surface temperature. This fit is performed from 1/4 to 1/2 preindustrial concentrations where the peak of the band emits in the troposphere, but the minimum of the band is optically thin to separate l from κ_0. Note that if all the wavenumbers in this band are optically thick, we instead take the area of a trapezoid by adding the area of a rectangle with width $\delta\nu_s^{em}$ and height $B(T_s) - B(T_1)$, where T_1 is the emission temperature at the edge of the band.

TABLE A3. Descriptions of parameters needed to model radiative forcing by CH_4.

Parameter	Description	Value	Source
τ^{em}	Emission optical thickness	0.82	Eq. (A1)
$\kappa_{thick} = \kappa_0 e^{-(\lvert\nu_0-\nu\rvert)/l}$	Thick band absorption coefficient	$\kappa_0 = 125$ m^2 kg^{-1} $\nu_0 = 1490$ cm^{-1} $l = 14$ cm^{-1}	Fit to LBL
κ_{thin}	Thin band absorption coefficient	0.5 m^2 kg^{-1}	Fit to LBL
ν^*	CH_4 band center	1305 cm^{-1}	LBL model
$\delta\nu$	CH_4 thin bandwidth	109.5 cm^{-1}	Fit to LBL

TABLE A4. Descriptions of parameters needed to model radiative forcing by N_2O.

Parameter	Description	Value	Source
$\tau^{em}_{\nu_2}$	ν_2 emission optical thickness	0.65	Eq. (A1)
$\tau^{em}_{2\nu_2}$	$2\nu_2$ emission optical thickness	0.84	Eq. (A1)
$\tau^{em}_{\nu_1}$	ν_1 emission optical thickness	0.86	Eq. (A1)
$\kappa_1 = \kappa_0 e^{-(\lvert\nu_0-\nu\rvert)/l}$	ν_1 band left triangle	$\kappa_0 = 70\ m^2\ kg^{-1}$ $\nu_0 = 1275\ cm^{-1}$ $l = 7.5\ cm^{-1}$	Fit to LBL
$\kappa_2 = \kappa_0 e^{-(\lvert\nu_0-\nu\rvert)/l}$	ν_1 band right triangle	$\kappa_0 = 70\ m^2\ kg^{-1}$ $\nu_0 = 1300\ cm^{-1}$ $l = 5.5\ cm^{-1}$	Fit to LBL

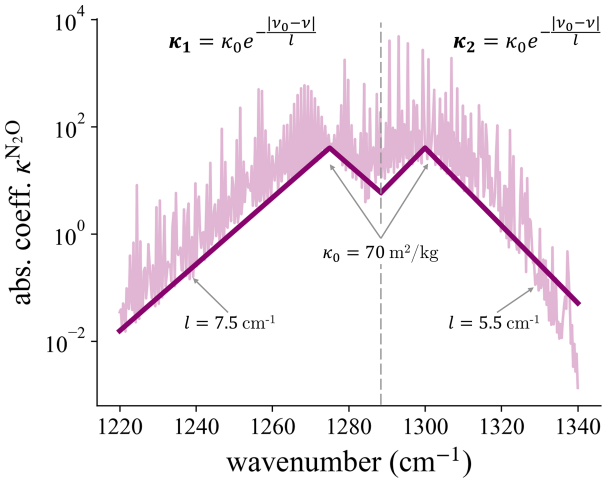

FIG. A3. The LBL N_2O absorption coefficient in the ν_1 band, with the idealized piecewise exponential-triangular reference coefficient drawn overtop. Relevant parameter values for the idealized absorption coefficient are labeled.

The optically thin band is modeled as a band-average absorption coefficient. We determine this coefficient as best representing the band-mean optical depth and resulting forcing and obtain $\kappa^{CH_4}_{thin} = 0.5\,m^2\,kg^{-1}$ (Fig. A2d).

Finally, we treat spectral overlap of water vapor with methane. Only line absorption is considered as it dominates overlap with the CH_4 band. The idealized H_2O absorption coefficient in the methane band is plotted in Fig. A2e, with numerical values in Table A1. The water vapor absorption coefficient is sorted according to the same index as the CH_4 absorption coefficient to preserve monochromaticity (not shown). As before, where water vapor emits in the troposphere, the surface temperature is replaced with the water vapor emission temperature in Eq. (19).

f. N_2O

We model only the 1220–1340 cm^{-1} band of N_2O as it is optically thick at preindustrial concentrations. A piecewise-triangular absorption coefficient described by peaks κ_0 and exponential falloff with slope l [Eq. (A3)] is fit as follows: First, slope coefficients l are fit in idealized isothermal atmospheres with differing surface temperatures. The isothermal atmosphere allows the forcing to be independent of κ_0 such that the slope coefficient l can be fit independently. This is similar to the fit of the CO_2 absorption coefficient in isothermal and varying stratospheres in Jeevanjee et al. (2021). Next, the slope coefficients are held constant, and the peak absorption coefficient κ_0 is fit in moist adiabatic atmospheres with varying surface temperature. The line-by-line and resulting idealized absorption coefficients are plotted in Fig. A3, and exact parameter values are listed in Table A4.

REFERENCES

Buehler, S. A., M. Brath, O. Lemke, Ø. Hodnebrog, R. Pincus, P. Eriksson, I. Gordon, and R. Larsson, 2022: A new halocarbon absorption model based on HITRAN cross-section data and new estimates of halocarbon instantaneous clear-sky radiative forcing. *J. Adv. Model. Earth Syst.*, **14**, e2022MS003239, https://doi.org/10.1029/2022MS003239.

——, and Coauthors, 2025: The atmospheric radiative transfer simulator ARTS, version 2.6—Deep python integration. *J. Quant. Spectrosc. Radiat. Transfer*, **341**, 109443, https://doi.org/10.1016/j.jqsrt.2025.109443.

Byrne, B., and C. Goldblatt, 2014: Radiative forcing at high concentrations of well-mixed greenhouse gases. *Geophys. Res. Lett.*, **41**, 152–160, https://doi.org/10.1002/2013GL058456.

Chiodo, G., and L. M. Polvani, 2022: New insights on the radiative impacts of ozone-depleting substances. *Geophys. Res. Lett.*, **49**, e2021GL096783, https://doi.org/10.1029/2021GL096783.

Dufresne, J.-L., V. Eymet, C. Crevoisier, and J.-Y. Grandpeix, 2020: Greenhouse effect: The relative contributions of emission height and total absorption. *J. Climate*, **33**, 3827–3844, https://doi.org/10.1175/JCLI-D-19-0193.1.

Elsasser, W. M., 1942: Heat transfer by infrared radiation in the atmosphere. Harvard Meteorological Studies 6, 108 pp., https://ia800306.us.archive.org/9/items/ElsasserFull1942/Elsasser-Full-1942_text.pdf.

Etminan, M., G. Myhre, E. J. Highwood, and K. P. Shine, 2016: Radiative forcing of carbon dioxide, methane, and nitrous oxide: A significant revision of the methane radiative forcing. *Geophys. Res. Lett.*, **43**, 12 614–12 623, https://doi.org/10.1002/2016GL071930.

Forster, P., and Coauthors, 2021: The Earth's energy budget, climate feedbacks, and climate sensitivity. *Climate Change 2021: The Physical Science Basis*, V. Masson-Delmotte et al., Eds., Cambridge University Press, 923–1054.

Fu, Q., and K. Liou, 1992: On the correlated *k*-distribution method for radiative transfer in nonhomogeneous atmospheres. *J. Atmos. Sci.*, **49**, 2139–2156, https://doi.org/10.1175/1520-0469(1992)049<2139:OTCDMF>2.0.CO;2.

Goody, R. M., and Y. L. Young, 1964: *Atmospheric Radiation.* Oxford University Press, 436 pp.

Gordon, I. E., and Coauthors, 2017: The HITRAN2016 molecular spectroscopic database. *J. Quant. Spectrosc. Radiat. Transfer*, **203**, 3–69, https://doi.org/10.1016/j.jqsrt.2017.06.038.

Hansen, J., I. Fung, A. Lacis, D. Rind, S. Lebedeff, R. Ruedy, G. Russell, and P. Stone, 1988: Global climate changes as forecast by Goddard institute for space studies three-dimensional model. *J. Geophys. Res.*, **93**, 9341–9364, https://doi.org/10.1029/JD093iD08p09341.

He, H., R. J. Kramer, B. J. Soden, and N. Jeevanjee, 2023: State dependence of CO_2 forcing and its implications for climate sensitivity. *Science*, **382**, 1051–1056, https://doi.org/10.1126/science.abq6872.

Hersbach, H., and Coauthors, 2023: ERA5 monthly averaged data on single levels from 1940 to present. Copernicus Climate Change Service (C3S) Climate Data Store (CDS), accessed 17 May 2024, https://doi.org/10.24381/cds.adbb2d47.

Hodnebrog, Ø., and Coauthors, 2020: Updated global warming potentials and radiative efficiencies of halocarbons and other weak atmospheric absorbers. *Rev. Geophys.*, **58**, e2019RG000691, https://doi.org/10.1029/2019RG000691.

Huang, Y., and M. Bani Shahabadi, 2014: Why logarithmic? A note on the dependence of radiative forcing on gas concentration. *J. Geophys. Res. Atmos.*, **119**, 13 683–13 689, https://doi.org/10.1002/2014JD022466.

——, X. Tan, and Y. Xia, 2016: Inhomogeneous radiative forcing of homogeneous greenhouse gases. *J. Geophys. Res. Atmos.*, **121**, 2780–2789, https://doi.org/10.1002/2015JD024569.

Jeevanjee, N., and S. Fueglistaler, 2020a: On the cooling-to-space approximation. *J. Atmos. Sci.*, **77**, 465–478, https://doi.org/10.1175/JAS-D-18-0352.1.

——, and ——, 2020b: Simple spectral models for atmospheric radiative cooling. *J. Atmos. Sci.*, **77**, 479–497, https://doi.org/10.1175/JAS-D-18-0347.1.

——, J. T. Seeley, D. Paynter, and S. Fueglistaler, 2021: An analytical model for spatially varying clear-sky CO_2 forcing. *J. Climate*, **34**, 9463–9480, https://doi.org/10.1175/JCLI-D-19-0756.1.

Kochanov, R. V., and Coauthors, 2019: REPRINT OF: Infrared absorption cross-sections in HITRAN2016 and beyond: Expansion for climate, environment, and atmospheric applications. *J. Quant. Spectrosc. Radiat. Transfer*, **238**, 106708, https://doi.org/10.1016/j.jqsrt.2019.106708.

Koll, D. D. B., N. Jeevanjee, and N. J. Lutsko, 2023: An analytic model for the clear-sky longwave feedback. *J. Atmos. Sci.*, **80**, 1923–1951, https://doi.org/10.1175/JAS-D-22-0178.1.

Liang, Y.-C., L. M. Polvani, M. Previdi, K. L. Smith, M. R. England, and G. Chiodo, 2022: Stronger arctic amplification from ozone-depleting substances than from carbon dioxide. *Environ. Res. Lett.*, **17**, 024010, https://doi.org/10.1088/1748-9326/ac4a31.

Liou, K.-N., 2002: *An Introduction to Atmospheric Radiation.* International Geophysics Series, Vol. 84, Elsevier, 608 pp.

May, R. M., and Coauthors, 2022: MetPy: A meteorological python library for data analysis and visualization. *Bull. Amer. Meteor. Soc.*, **103**, E2273–E2284, https://doi.org/10.1175/BAMS-D-21-0125.1.

Pierrehumbert, R. T., 2010: *Principles of Planetary Climate.* Cambridge University Press, 652 pp.

Pincus, R., P. M. Forster, and B. Stevens, 2016: The Radiative Forcing Model Intercomparison Project (RFMIP): Experimental protocol for CMIP6. *Geosci. Model Dev.*, **9**, 3447–3460, https://doi.org/10.5194/gmd-9-3447-2016.

——, and Coauthors, 2020: Benchmark calculations of radiative forcing by greenhouse gases. *J. Geophys. Res. Atmos.*, **125**, e2020JD033483, https://doi.org/10.1029/2020JD033483.

Pinnock, S., M. D. Hurley, K. P. Shine, T. J. Wallington, and T. J. Smyth, 1995: Radiative forcing of climate by hydrochlorofluorocarbons and hydrofluorocarbons. *J. Geophys. Res.*, **100**, 23 227–23 238, https://doi.org/10.1029/95JD02323.

Polvani, L. M., M. Previdi, M. R. England, G. Chiodo, and K. L. Smith, 2020: Substantial twentieth-century arctic warming caused by ozone-depleting substances. *Nat. Climate Change*, **10**, 130–133, https://doi.org/10.1038/s41558-019-0677-4.

Ramanathan, V., 1975: Greenhouse effect due to chlorofluorocarbons: Climatic implications. *Science*, **190**, 50–52, https://doi.org/10.1126/science.190.4209.50.

Romps, D. M., J. T. Seeley, and J. P. Edman, 2022: Why the forcing from carbon dioxide scales as the logarithm of its concentration. *J. Climate*, **35**, 4027–4047, https://doi.org/10.1175/JCLI-D-21-0275.1.

Schmithüsen, H., J. Notholt, G. König-Langlo, P. Lemke, and T. Jung, 2015: How increasing CO_2 leads to an increased negative greenhouse effect in Antarctica. *Geophys. Res. Lett.*, **42**, 10 422–10 428, https://doi.org/10.1002/2015GL066749.

Schwarzschild, K., 1906: On the equilibrium of the sun's atmosphere. *Nachrichten Von Der Königlichen Gesellschaft Der Wissenschaften Zu Göttingen. Math.-Phys. Klasse*, **195**, 41–53.

Seeley, J. T., 2018: Convection, radiation, and climate: Fundamental mechanisms and impacts of a changing atmosphere. M.S. thesis, Dept. of Philosophy in Earth and Planetary Sciences, University of California, 145 pp.

Shine, K. P., 1991: On the cause of the relative greenhouse strength of gases such as the halocarbons. *J. Atmos. Sci.*, **48**, 1513–1518, https://doi.org/10.1175/1520-0469(1991)048<1513:OTCOTR>2.0.CO;2.

Smith, K. L., G. Chiodo, M. Previdi, and L. M. Polvani, 2018: No surface cooling over Antarctica from the negative greenhouse effect associated with instantaneous quadrupling of CO_2 concentrations. *J. Climate*, **31**, 317–323, https://doi.org/10.1175/JCLI-D-17-0418.1.

Stephens, G. L., 1994: *Remote Sensing of the Lower Atmosphere: An Introduction.* Oxford University Press, 523 pp.

Stevens, B., and L. Kluft, 2023: A colorful look at climate sensitivity. *Atmos. Chem. Phys.*, **23**, 14 673–14 689, https://doi.org/10.5194/acp-23-14673-2023.

Wilson, D. J., and J. Gea-Banacloche, 2012: Simple model to estimate the contribution of atmospheric CO_2 to the Earth's greenhouse effect. *Amer. J. Phys.*, **80**, 306–315, https://doi.org/10.1119/1.3681188.

Wordsworth, R., J. Seeley, and K. P. Shine, 2024: Fermi resonance and the quantum mechanical basis of global warming. *Planet. Sci. J.*, **5**, 67, https://doi.org/10.3847/PSJ/ad226d.

Zhang, Y., N. Jeevanjee, and S. Fueglistaler, 2020: Linearity of outgoing longwave radiation: From an atmospheric column to global climate models. *Geophys. Res. Lett.*, **47**, e2020GL089235, https://doi.org/10.1029/2020GL089235.